Chem Soc Rev

REVIEW ARTICLE

View Article Online
View Journal | View Issue

Cite this: *Chem. Soc. Rev.*, 2017, **46**, 5903

Quantum cascade lasers (QCLs) in biomedical spectroscopy

Andreas Schwaighofer, [a] Markus Brandstetter [b] and Bernhard Lendl *[a]

Quantum cascade lasers (QCL) are the first room temperature semiconductor laser source for the mid-IR spectral region, triggering substantial development for the advancement of mid-IR spectroscopy. Mid-IR spectroscopy in general provides rapid, label-free and objective analysis, particularly important in the field of biomedical analysis. Due to their unique properties, QCLs offer new possibilities for development of analytical methods to enable quantification of clinically relevant concentration levels and to support medical diagnostics. Compared to FTIR spectroscopy, novel and elaborated measurement techniques can be implemented that allow miniaturized and portable instrumentation. This review illustrates the characteristics of QCLs with a particular focus on their benefits for biomedical analysis. Recent applications of QCL-based spectroscopy for analysis of a variety of clinically relevant samples including breath, urine, blood, interstitial fluid, and biopsy samples are summarized. Further potential for technical advancements is discussed in combination with future prospects for employment of QCL-based devices in routine and point-of-care diagnostics.

Received 2nd June 2017

DOI: 10.1039/c7cs00403f

rsc.li/chem-soc-rev

1. Introduction

The mid-IR region (400–4000 cm^{-1}) with strong fundamental rotational–vibrational transitions offers highly discriminatory information inherently allowing molecule-specific detection. With the first realization of QCLs in 1994, the way was paved for the development of compact, room temperature operated semiconductor lasers in this analytically attractive spectral region. Unlike previously existing mid-IR lasers, such as CO_2 and lead salt lasers as well as light sources based on optical parametric generation (difference frequency generation, DFG; and optical parametric oscillation, OPO), QCLs combine wide tunability, stable operation at room temperature and versatility in pulsed and CW mode with modulation capability up to the MHz-regime. Compared to thermal light sources employed in

[a] *Institute of Chemical Technologies and Analytics, Vienna University of Technology, Getreidemarkt 9/164, 1060 Vienna, Austria. E-mail: Bernhard.Lendl@tuwien.ac.at*
[b] *Research Center for Non Destructive Testing GmbH, Altenbergerstraße 69, 4040 Linz, Austria*

Andreas Schwaighofer

Andreas Schwaighofer is a post-doctoral researcher at the Institute of Chemical Technology and Analytics at the Technische Universität Wien, Austria. He studied chemical engineering at the Johannes Kepler University in Linz and Virginia Commonwealth University in Richmond, VA, USA. In 2013, he received his PhD from the University of Natural Resources and Life Sciences, Vienna, Austria. His work focuses on applying spectroscopic methods to study the stability and structural changes of proteins upon external perturbation, ligand binding and denaturation. Currently, his research interests include QCL-IR transmission spectroscopy for protein analysis and application of laser-based IR spectroscopy to biomedical applications.

Markus Brandstetter

Markus Brandstetter received his Master's degree in Physics and his PhD in Chemistry from the Technische Universität Wien. In his Master thesis, he worked on the combination of ultrasonic particle manipulation with mid-IR spectroscopy. During his PhD, he specialized on the characterization and application of quantum cascade lasers for mid-IR spectroscopy with a focus on blood analysis. In 2014, he joined the RECENDT GmbH as Head of the Infrared and Raman Spectroscopy group, where he and his team are working on spectroscopic sensing technologies employing QCLs, mid-IR supercontinuum sources and MEMS-based near-IR and mid-IR micro-spectrometers.

conventional FTIR spectrometers, QCLs offer coherent and polarized light with an increased spectral power density by a factor of 10^4 and more. Advances in technological aspects and wide availability of QCLs led to development of new measurement schemes[1] and employment in diverse fields of application such as industrial process monitoring, security and biomedical sensing.

Mid-IR spectroscopy has been broadly applied for analysis of clinically relevant samples.[2–8] This spectral region provides rich information about biomedical samples that are mainly composed of proteins, lipids, carbohydrates and deoxyribonucleic acids.[9] The intended purpose of analytical methods for biomedical diagnostics is to provide the practitioner with tools to efficiently determine the presence and cause of disease in order to select the most appropriate intervention, thus improving patient health care *via* better diagnosis, prognosis and surveillance. From the analytical perspective, methods for application in a clinical setting need to fulfil the respective figures of merit in terms of analytical chemistry such as sensitivity, limit of detection (LOD), repeatability and reproducibility. From the medical viewpoint, an analytical approach needs to meet the criteria regarding statistical evaluation of diagnostic performance including receiver operator characteristic (ROC) curves and specificity as appropriate for the respective diagnostic field.[10]

Furthermore, requirements for analytical instruments designated for clinical use comprise robust and easy use (operation by untrained staff), feasibility to provide results in a timely manner (little sample preparation, short time between test and diagnosis), capability for miniaturization and portability (relevant for field tests and home use), potential for integration (point-of-care diagnostics) and, last but not least affordable costs. Particularly appealing in this regard is the prospect of non-destructive, label-free measurements that opens the possibility for non-invasive diagnostics and real-time monitoring.

The aim of developing QCL-based methods for biomedical diagnostics is not only to adopt procedures already established for FTIR spectroscopy, but perform better than these techniques and even expand into new fields and modes of application that have now become feasible due to the unique properties of these light sources. First QCLs had their applications in gas-phase analysis, which found broad distribution in industrial and atmospheric monitoring and made use of the inherent possibility of laser modulation that enabled advanced measurement schemes beyond conventional absorption spectroscopy. Methods for trace gas analysis have been adapted for breath analysis and low concentrations of breath compounds became detectable that were not accessible by FTIR spectroscopy. Since the availability of broadly tunable QCLs, there have been an ever growing number of applications in the liquid-phase. High emission powers of QCLs permit large path lengths for robust transmission measurements even in the presence of water, the ubiquitous solvent of biological samples. The broad spectral tunability facilitates the use of chemometric methods that enable accurate multi-component quantification even in a complex sample matrix. Regarding clinical applications, this signified the possibility for rugged automatization of direct measurements of bodily fluids. For IR microscopy of biopsy samples, the emergence of QCLs allowed an entirely new data acquisition scheme, *i.e.* discrete frequency imaging, where data is collected of only a few chosen wavenumbers that have been identified as significant for the diagnostic problem. Together with the feasibility to employ thermoelectrically-cooled microbolometers with larger field of view, QCL-based IR microscopy permits shorter acquisition times compared to FTIR microscopy.

Apart from the metrological benefits of QCLs, they allow to implement new techniques for biomedical analysis that may lead to direct amenities for the patient and additional information for the physician. In blood glucose monitoring, a non-invasive approach has been developed on grounds of QCL-based photoacoustic and photothermal spectroscopy, probing the glucose level in the interstitial fluid through skin. In breath analysis, which is inherently non-invasive, QCL-based sampling techniques can provide time-resolved data in real-time. In histopathology, since the staining step can be omitted for IR microscopic analysis and through applying accelerated data acquisition schemes enabled by QCLs, as described above, the time between biopsy and diagnosis can significantly be reduced.

This review aims at providing an exhaustive overview of current applications of QCLs, working towards or already embedded in a clinical setting. Initially, operation principles of different types of QCLs are briefly outlined followed by a discussion of the unique properties that are provided by these light sources. The main part summarizes biomedical applications of QCLs segmented into the fields of breath analysis, microscopic tissue and biofluid screening as well as analysis of bodily fluids.

Bernhard Lendl

Bernhard Lendl received his PhD degree in Technical Chemistry from Technische Universität Wien (TU Wien) in 1996. His research focuses on advancing analytical sciences through the development of novel analytical techniques and instrumentation based on infrared and Raman spectroscopy and their application to environmental and process analytical chemistry, material characterization as well as bio-medical diagnostics. In 2008, he co-founded the TU Wien spin-off company QuantaRed Technologies GmbH, which develops mid-IR laser based analyzers for liquids. Since 2011, he heads the research division on environmental and process analytical chemistry at TU Wien where he was appointed full professor for Vibrational Spectroscopy in 2016.

2. Quantum cascade lasers as mid-IR light sources

2.1. Operation principles

Lasers (Light Amplification by Stimulated Emission of Radiation) are sources of coherent radiation based on stimulated emission

of photons. Unlike naturally occurring light sources, typically emitting thermal radiation following the Planck radiation law, laser radiation exhibits high coherence, both in terms of frequency and space. As a result, high spectral power densities are achieved, representing a significant advantage in many spectroscopic techniques.

For laser operation, two conditions need to be met: population inversion of the electronic states in the active medium and optical feedback by a resonator.[11] QCLs represent a subgroup of electrically pumped semiconductor lasers. Whereas conventional semiconductor lasers generate photons by radiative recombination of electrons from the conduction band with holes from the valence band (inter-band transitions), in QCLs emission is achieved by inter-subband transitions of electrons within the semiconductors conduction band. QCLs comprise a series of layers of different semiconductor materials exhibiting varying band gaps (hetero-structure) that are precisely defined both in terms of composition and thickness in the nanometer range. In conventional lasers, the emission wavelength is determined by the band gap energy of the utilized materials, thus restricting their application mainly to the UV-vis and near-IR (NIR) range. In QCLs, the emission wavelength is decoupled from the band gap of the semiconductor material. As the transitions arise between confined quantum states, the emission energy can be tailored by adjusting the layer thickness and material properties in a wide region to the particular need while keeping the same heterostructure materials.[12–14]

Upon application of an electrical field in the order of 50 kV cm^{-1}, electrons are injected into the upper state of the quantum well system. The subsequent radiative electron relaxation into a lower inter-subband state generates mid-IR photons with an energy corresponding to the energy difference between initial and final state (Fig. 1A). Thus, the energy spacing of the optical transition determines the wavelength of the emitted photon. The selection rule for optical transitions implies that only modes with electrical vector parallel to the growth direction (TM polarized modes) participate in the laser action, hence edge emitting QCLs emit polarized light. These optical transitions take place in the active regions, whereas the injector regions maintain population inversion. This is achieved by extraction of electrons from the active region by resonant tunnelling subsequently to optical transition. The extraction process occurs approx. ten times faster than the radiative transition, hence electrons accumulate in the subsequent injector region, thereby preserving population inversion. In QCLs, a cascade of typically up to 40 repetitions of this characteristic active region-injection sequences is realized, thus a single electron can undergo multiple radiative transitions generating mid-IR photons (“electron recycling”), in contrast to diode lasers, where each electron results in single-photon emission only.[15–17]

This concept obtaining optical gain from intra-band electron transitions was suggested in 1971 by Kazarinov and Suris.[18] The first QCL was realized in 1994 by Faist *et al.* at Bell Labs (USA).[19] Experimental realization of the heterostructure design was facilitated by new crystal growth technologies such as molecular beam epitaxy (MBE) or metal–organic vapor phase epitaxy (MOVPE) allowing for manufacturing of crystalline heterostructures with

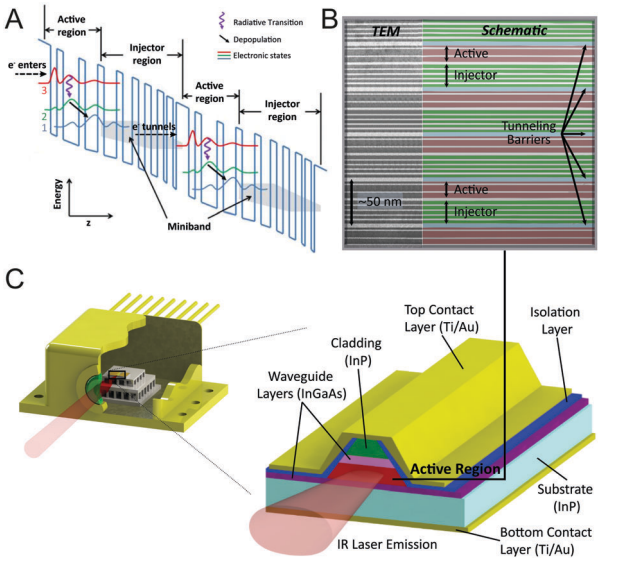

Fig. 1 (A) Schematic band diagram illustrating two stages of the cascaded quantum well structure of a QCL with each stage consisting of an active and an injector region. Radiative transitions occur between states 3 and 2 in the active regions. Population inversion is maintained after rapid depopulation of lower state 2 into state 1 which couples strongly with the minibands formed in the injector regions that facilitate e^--tunnelling to state 3 in the next stage. Reproduced from ref. 245 with permission from InTech, copyright 2010. (B) TEM image of a partial section of the active region in a 3-quantum well design QCL. Reproduced from ref. 246 with permission from IEEE, copyright 2008. (C) Sketch showing cross section and material composition of a processed QCL ridge.

atomic level resolution (see Fig. 1B). In the processed QCL ridge, electrons are injected *via* the top and bottom contact layers, and then tunnel through the gain medium (active region), where mid-IR photon emission perpendicular to the layer plane is achieved (see Fig. 1C). The cladding layers act as electrical contacts to the active region. The total thickness is in the order of 4 to 8 μm, whereas the active region itself accounts for 1 to 4 μm.

Along with the layout of the active medium, the design of the resonator is of significant importance. In the resonator, the mid-IR electromagnetic waves of the laser chip propagate and get amplified, if the appropriate optical feedback is provided. In this way, stimulated emission is achieved. An in-depth discussion of the underlying physical principles and quantitative analysis of QCL operation is beyond the scope of this review article, however, a number of reviews were dedicated to this particular topic.[12,15,20,21]

Compared to other laser light sources in the mid-IR region, the described operation principle has significant implications on the emission parameters. Most importantly, there is the possibility of tailoring the emission wavelength independently from the bandgaps of available materials by adapting the thicknesses of the respective layers. The wavelength can be freely designed over almost 3 octaves of the photon emission frequencies using one single material system as active medium. While the material system based on InGaAs/AlInAs heterostructure grown on InP substrate is the most mature technology and compatible with mass production requirements,[22] recently new

active region designs based on InAs/AlSb have been presented.[23] The position of the emission center wavelength of a laser within the mid-IR region is determined by the energy difference of the two energy states corresponding to the intra-band radiative transition (see Fig. 1A). On the low frequency side of the IR region (currently approx. ν = 351 cm^{-1} or λ = 28.5 μm),[24] the limit is given by competing phonon transitions at the edge of the Reststrahlenband. At high frequencies (currently approx. ν = 3300 cm^{-1} or λ = 3 μm),[25] the limit is given by the maximum band-offset achievable using InGaAs/AlInAs heterostructures grown on InP substrates. Thus, the entire mid-IR region is accessible with QCLs, in most cases at room temperature conditions. Furthermore, QCLs operated with thermoelectric or liquid nitrogen cooling are available in the far-IR.[26] The flexibility thus provided by QCLs constitutes a main advantage for targeted spectroscopy and can only be surpassed by free electron lasers.[27]

Apart from the location of the center wavelength (*i.e.* position of the gain maximum), the width of the gain curve is a parameter that can be tailored in QCLs. Designs based on a continuum of the states on the low-energy end of the optical transition (bound-to-continuum design) instead of only two discrete levels have paved the way for extending the gain width beyond the known possibilities of semiconductor lasers and solid state lasers in general.[20,28,29] Broadband gain media of bound-to-continuum QCLs are mostly used in tunable external cavity (EC) lasers enabling spectral coverage of more than several hundred wavenumbers.[30]

In addition to the emission wavelength and spectral tuning range, the spectral coherence of the emitted radiation is an important parameter. A narrow laser linewidth is required particularly in gas-phase analysis to achieve high selectivity for resolving different species that have similar ro-vibrational frequencies.[31–33] In QCLs, this preferred single mode emission is not inherently obtained due to the fast gain recovery that occurs in the picosecond range. Thus, the gain recovery process is faster than carrier diffusion, and spatial hole burning is dominant, favoring multimode operation.[34] However, single mode emission can be achieved by incorporating a frequency filter or mode selector, *e.g.* grating into the laser system cavity.

2.2. Types of QCLs and their field of applications

QCLs are generally classified by means of the resonator design. The three common types of laser resonators are Fabry Pérot (FP), distributed feedback (DFB) and external cavity (EC), see Fig. 2. Depending on the configuration, the overall gain provided by the active region is reduced by the sum of all losses related to the respective resonator design. Losses include unavoidable losses, *e.g.* waveguide losses due to light propagation in the laser chip, and mirror losses stemming from the facets, as well as losses that are introduced on purpose for selecting specific emission wavelengths within the available gain curve. The latter can be a wavelength-selective grating, which is either integrated in the laser chip itself (Bragg grating) or realized as an external diffraction grating.[15]

The Fabry–Pérot (FP) design is the simplest resonator configuration consisting of the bare QCL chip with high

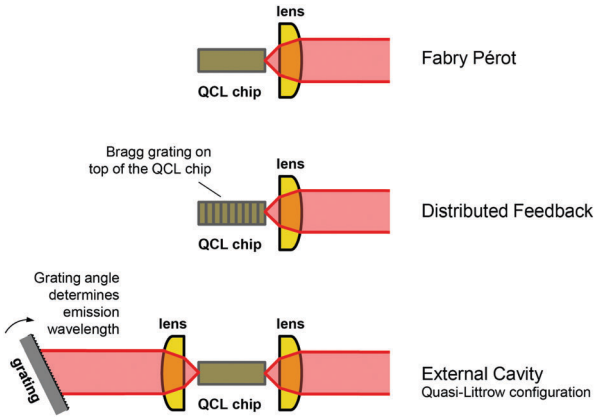

Fig. 2 Common configurations of QCLs.

reflection coatings on the end facets of the laser ridge. Sufficient gain must be provided by the active material and the distance between the mirrors must allow constructive interference to meet the conditions for light amplification. Hence, the determining parameter in a FP configuration is the cavity length. However, the standing wave condition is fulfilled for a large number of longitudinal modes, resulting in multimode emission over a wide spectral range with hundreds of longitudinal modes.[34,35] These emission characteristics are disadvantageous for most spectroscopic applications, particularly in the gas-phase, where single mode emission is preferred. Nevertheless, FP-QCLs have been applied for liquid-phase analysis, where absorption bands are much broader.[36,37] Further, it has been proposed to use this type of QCLs in frequency combs[38] and as multi-mode CW source for FTIR spectroscopy replacing conventional low-power globars.[39]

In DFB-QCLs, a Bragg grating is integrated into the laser waveguide along the light propagation direction, thus selecting a single mode within the gain provided by the active medium.[12,29] This selection mechanism leads to increased losses for all modes except the one the grating was designed for. The emission wavelength of DFB-QCLs is tunable within a range of approx. 5 cm^{-1} by changing the injection current and/or the operation temperature.[40] Both methods of tuning lead to a change in the effective refractive index of the laser chip material and thus shift the resonance wavelengths of the Bragg grating, with a tuning rate approx. 0.1–0.2 cm^{-1} K^{-1}.[12] This type of QCL is available as standard ridge, multi-segment array, and ring-design. Most commercial DFB-QCLs are configured as ridge lasers which are designed for facet edge emission. The associated disadvantage of a beam divergence in the range of a few tens of degrees needs to be corrected by collimation optics. Due to its narrowband single-mode emission, this type of QCL is the most commonly used for gas measurements.[41–43] In order to achieve broader spectral coverage in the range of several tens of wavenumbers featuring a spectral resolution of better than 0.01 cm^{-1} (300 MHz), multiple DFB ridges can be combined to obtain a DFB-QCL array.[44–47] Potential applications for this multi-wavelength QCL light source may be in the analysis of liquid analytes, where broad spectral ranges need to be

covered[48] or for analysis of multiple gas species. DFB-QCLs have been further implemented in form of ring-cavity surface emitting (RCSE) QCLs,[49] where wavelength selection and surface emission are enabled by radial second-order Bragg gratings etched on top of the ring cavity. This type of laser is characterised by mode-hop-free operation and beam stability during operation combined with a low threshold current density.[50,51] Compared to conventional laser types, RCSE-QCLs exhibit larger tuning ranges (up to 10.8 cm^{-1}), lower lasing thresholds and a higher optical output power due to the absence of facet losses.[51] Low beam divergence of only a few degrees facilitates coupling of the emitted light into an optical system.[52] RCSE-QCLs have been employed for gas measurements in process analytics.[53]

In contrast to the DFB approach, where a fixed emission wavelength is selected by an integrated Bragg grating, the external cavity (EC) design enables broadband spectral tuning by an external diffraction grating.[22] Changing the angle of the diffraction grating relative to the QCL chip allows tuning ranges of up to several hundred wavenumbers. Hence, three parameters determine the mode spectrum of an EC-QCL: the QCL chip FP modes, the external cavity FP modes as well as the reflectivity spectrum of the external grating. In total, this leads to a broad emission curve with a superimposed fine structure.[54] First EC-QCLs featuring spectral coverage of approx. 35 cm^{-1} at cryogenic temperatures have been introduced in 2001.[55] Subsequent developments enabled room-temperature operation[56,57] and in current state-of-the-art EC-QCLs, the spectral coverage of a single chip could be extended to a maximum of 556 cm^{-1} in the 3–4 μm region[58] and 432 cm^{-1} in the 7.6–11.4 μm region.[21] Even larger tuning ranges of more than 1000 cm^{-1} provided by a single device can be achieved by beam combination of up to four individual EC-QCL modules, as commercially available by Block Engineering (Marlborough, USA), Daylight Solutions (San Diego, USA) and Pranalytica (Santa Monica, USA). For their latest models, tuning rates of up to 25 000 cm^{-1} s^{-1} (LaserTune, Block Engineering) and 5000 cm^{-1} s^{-1} (MIRcat-QT, Daylight Solutions) have been specified.

Regarding their emission characteristics, EC-QCLs are available in pulsed, standard continuous wave (CW) and mode-hop-free (MHF)–CW configurations. Pulsed and standard CW operation allow largest spectral tuning ranges and are frequently used for condensed phase spectroscopy and have found their applications in far-field[59] as well as near-field[60,61] infrared microscopy, stand-off measurements of solid residues[62] as well as in analysis of liquids.[63–65] However, these configurations might cause problems in high resolution gas-phase spectroscopy due to mode-hops that can occur during tuning.[54] Mode-hops originate from competition of different optical modes for the available net gain in the laser medium. Consequently, laser emission "hopping" from one mode to another, although the gain spectrum itself is homogeneous, may lead to distinctive gaps in the emission curve with associated laser noise.[66–68] To achieve mode-hop-free tuning, a mode tracking system has been developed for precisely matching the EC length and diffraction grating angle during the tuning process.[54] Here, drifts in laser emission power over time remain a difficulty for trace gas analysis. The additional expenditures required for MHF operation result in smaller spectral coverage and lower tuning rates.[69,70]

2.3. Specific properties of QCLs relevant for applied spectroscopy

The fundamentally different nature of quantum cascade lasers provides unique properties in comparison to other mid-IR light sources. QCLs provide coherent and polarized light at high spectral power densities. Furthermore, they can be operated at room temperature with versatile operation modes and with narrow spectral linewidth.[71] In the following, practical implications on spectroscopic applications arising from these unique characteristics will be discussed.

The spectral power provided by QCLs (mW–W range) is several orders of magnitude higher than that of globars employed in FTIR spectrometers (μW range).[13,63] The resultant increase of the measurement signal can either be proportional to the emission power, *e.g.* in case of photoacoustic detection,[72] or logarithmic by increasing the achievable optical path length in case of direct absorption spectroscopy, due to the exponential attenuation of the signal intensity according to Beer–Lambert's law. When comparing QCL-based spectroscopy with FTIR spectroscopy in terms of signal-to-noise ratio (SNR), the noise level introduced by low intensity thermal light sources in FTIR spectrometers can usually be neglected. Furthermore, FTIR spectroscopy benefits from the Fellgett's advantage (all wavelengths passing through the sample simultaneously) and the Jaquinot's advantage (higher light throughput than in passive dispersive techniques, where a monochromator slit is needed) that partially compensate for the low optical powers provided by thermal emitters. High intensity laser sources, on the other hand, contribute to the overall measurement noise, particularly when operated in pulsed mode due to pulse-to-pulse intensity fluctuations. This partially cancels out the signal-enhancement due to the substantial increase in optical path length enabled by QCLs in liquid-phase transmission measurements.[64,73,74] When applying an thermoelectrically-cooled detector, the SNR turned out to be similar to state-of-the-art FTIR spectrometers equipped with a liquid nitrogen-cooled detector.[64,74] In mid-IR microscopy, QCL powered imaging systems allow 150 times faster spectral data acquisition at equivalent SNR at comparable spectral and lateral resolution.[75]

For high spectral resolution applications, the field is dominated by DFB-QCLs and EC-QCLs in single-mode operation.[55,76] The narrow-linewidth emission offers high selectivity, high sensitivity and enable multiple-species sensing that is particularly desirable in trace-gas sensing. In conventional FTIR spectroscopy, improvement of the spectral resolution comes along with increased instrument dimensions due to the inverse proportionality between the resolution and the travelling range of the moving mirror. Standard FTIR laboratory spectrometers offer resolutions of approx. 0.06 cm^{-1} (*e.g.* Vertex 80, Bruker Optics). In single-mode laser based systems the spectral resolution is basically limited by the laser line width. QCLs offer particularly small linewidths even compared to other laser sources in the mid-IR spectral range, owing to their symmetric gain curve.[71] Laser linewidths are commonly

expressed in Hz, however, in mid-IR spectroscopy cm^{-1} are preferred as unity. Single mode emitting QCLs typically provide linewidths of <30 MHz (<0.001 cm^{-1}).[12] Particularly small linewidths of <10 Hz ($\sim 3 \times 10^{-9}$ cm^{-1}) were realized by locking QCLs to optical cavities.[77,78]

State-of-the-art QCLs can be operated in CW and pulsed mode at room temperature without cryogenic cooling but employing thermoelectric temperature control. Both operation modes have their advantages and limitations. Generally, the spectral coverage of a laser is larger when operated in pulsed operation compared to CW mode. For gas-phase analysis, CW operation is preferable as narrower linewidths can be achieved.[13,79] Further, CW operation allows to implement enhanced modulation techniques that can further improve the sensitivity of measurements.[80,81] Pulsed operation suffers from pulse-to-pulse intensity fluctuations,[82,83] but requires lower energy and no water cooling, consequently this mode may be preferential for portable devices.[80] When performing measurements in the condensed phase (liquid or bulk), larger absorption values can lead to excess heat transfer to the sample, which is undesired in direct absorption measurements.[63] Hence, pulsed mode operation can be considered as more attractive, as low average power avoid unwanted heat transfer to the sample which would lead to sample alteration, whereas high peak power levels allow for large optical path lengths in transmission measurements.[74,83,84]

Another effect observed in pulsed operation is a frequency downchirp of the QCL emission during each pulse caused by internal Joule heating. This effect is utilized, *e.g.* in intra-pulse spectroscopy by tuning over narrow gas absorption bands combined with a time-resolved measurement of the absorption using a fast detector.[85] The spectral downchirp is usually in the range of a few wavenumbers for ridge-type DFB-QCLs and slightly higher for RCSE-QCLs.[51] QCL-IR microscopy measurements of biological samples have been performed in CW[86,87] as well as in pulsed[59,88] operation mode.

The coherent nature of QCL emission enables advanced measurement schemes beyond conventional direct absorption measurements such as optical heterodyne detection[38,89–91] or Mach–Zehnder interferometry.[92–94] Further, an optical coherence tomography (OCT) system in the mid-IR region based on a QCL has been realized.[95,96] The improved characteristics of QCLs enabled the implementation of frequency combs[97] that provide an emission spectrum composed of a set of modes that are perfectly equally-spaced and have a well-defined phase relationship between each other.[98,99] In molecular spectroscopy, these optical sources have been employed for dual-comb spectroscopy that is based on the generation of a multi-heterodyne beating between two frequency combs with slightly different repetition frequencies. A detector measures the multi-heterodyne beat that contains information regarding the sample absorption at the optical frequency of the comb line.[100] Employing this technique, broadband (15 cm^{-1}), high resolution (80 MHz, 0.0027 cm^{-1}) spectra in the gas phase have been acquired at very short acquisition times (μs) and no moving parts.[101] Most recently, a commercial instrument based on this principle has become available (IRspectrometer, IRsweep).

Finally, radiation emitted by QCLs is linearly polarized, oriented perpendicular to the layered structure of the active region. This polarization origins in the quantum mechanical selection rules associated with inter-subband transitions.[102,103] Polarized light offers the possibility of enhanced selectivity, *e.g.* for the analysis of enantiomers and sensitivity, *e.g.* for Doppler-free polarization spectroscopy.[32,104] For determining the stereochemistry of chiral molecules by vibrational circular dichroism, the polarization of the QCL was externally modulated between left- and right-circular states by use of an photoelastic modulator.[105] *In situ* polarization control of QCL emission by facet engineering has been reported by using metallic gratings as plasmonic polarizers[106–108] or by integrated polarization mode converters in the laser waveguide.[109]

3. Application of QCLs in biomedical diagnostics

The works presented in this section illustrate a snapshot of the current state of biomedical implementations of QCLs in breath analysis, IR imaging for histopathology and biofluid screening as well as analysis of bodily fluids. Table 1 gives a summary of the applications. There were developed and published a large number of techniques and approaches for QCL-based analysis of specifically prepared samples that contain biological molecules. However, in the following, this review focusses on providing an overview of reports that detect clinically relevant parameters in the actual matrix, preferably even directly derived from a donor sample.

3.1. QCL-IR spectroscopy for breath analysis

Recent developments have made QCL-based detection schemes viable alternatives for exhaled breath analysis. Non-invasive and safe operation for both, the patient and personnel, easy use and the ability to early detect pathogenic changes at molecular level are the main advantage of breath testing. Traditionally, sensitive gas analysis was dominated by mass spectroscopy (MS), proton transfer reaction-MS and gas chromatography (GC). These analytical techniques come along with high size and cost as well as complicated maintenance routines that impede mobile and real-time online investigations.[110] Alternatively, low cost devices such as pellistors and semiconductor or electrochemical sensors provide sensitivity in the low ppm range, but suffer from low selectivity.[111] Within clinical diagnostics, breath analysis holds a unique position, as there is basically unlimited supply for continuous sampling together with availability within a short time frame unlike other bodily fluids such as blood or urine, whose production and thus collection is limited.[112] Accordingly, time-resolved and even real-time monitoring of exhaled breath is feasible and has become a desired parameter for analytical techniques employed in this field, along with distinct sensitivity and selectivity. The breath matrix (99.99%) is composed of nitrogen, oxygen, carbon dioxide and argon. The remaining volume (~ 100 ppm) consists of a mixture of approx. 500 different compounds, each present at concentration in the

Table 1 Summary of QCL applications in biomedical spectroscopy

Breath analysis

Analyte	Spectroscopic technique	QCL type	QCL operation mode	Citations
$^{12}CO_2/^{13}CO_2$	Multipass AS	DFB-QCL	Pulsed	Weidmann *et al.*, 2005[128]
	AS	DFB-QCL	Pulsed	Rubin *et al.*, 2011[129]
	AS	DFB-QCL	CW	Kasyutich *et al.*, 2012[130]
	Hollow core waveguide	EC-QCL	Pulsed	Wörle *et al.*, 2013[131]
Acetone	CE-AS	DFB-QCL	CW	Ciaffoni *et al.*, 2012[136]
	AS	EC-QCL	Pulsed	Reyes-Reyes *et al.*, 2015[137]
Carbon monoxide (CO)	Multipass AS	DFB-QCL	Pulsed	Moeskops *et al.*, 2006[140]
	OA-ICOS, 2*f*/1*f*-WMS	DFB-QCL	CW	Pakmanesh *et al.*, 2016[141]
	Multipass 2*f*-WMS	EC-QCL	CW	Ghorbani *et al.*, 2017[142]
Ammonia (NH_3)	CRDS	DFB-QCL	Pulsed	Manne *et al.*, 2006[145]
	Multipass AS	DFB-QCL	Pulsed	Manne *et al.*, 2009[146]
	2*f*-WM-QEPAS	DFB-QCL	CW	Lewicki *et al.*, 2011[147]
	2*f*-WM-QEPAS	DFB-QCL	CW	Tittel *et al.*, 2011[148]
	2*f*-WM-QEPAS	DFB-QCL	CW	Tittel *et al.*, 2012[149]
	2*f*/1*f*-WMS	DFB-QCL	CW	Owen *et al.*, 2014[150]
Nitric oxide (NO)	Multipass AS, CE-AS	DFB-QCL	CW	Menzel *et al.*, 2001[155]
	Multipass 2*f*-WMS	DFB-QCL	CW	Cristescu *et al.*, 2008[156]
	Multipass 2*f*-WMS	DFB-QCL	CW	Mandon *et al.*, 2012[157]
	2*f*-WMS-OA-ICOS	DFB-QCL	CW	Bakhirkin *et al.*, 2004[158]
	ICOS, CRDS	DFB-QCL	Pulsed	Silva *et al.*, 2005[159]
	ICOS	DFB-QCL	CW	McCurdy *et al.*, 2006[160]
	ICOS	DFB-QCL	CW	McCurdy *et al.*, 2007[161]
	ICOS	DFB-QCL	CW	Marchenko *et al.*, 2013[162]
	CEAS	DFB-QCL	Pulsed	Wojtas, 2015[163]
	CRDS	EC-QCL	CW	De *et al.*, 2016[164]
$^{14}NO/^{15}NO$	FRS spectroscopy	DFB-QCL	CW	Wang *et al.*, 2015[132]
NO, CO, N_2O, CO_2	Multipass AS	DFB-QCL	Pulsed	Shorter *et al.*, 2010[163]
Multicomponent	Multipass AS	EC-QCL	Pulsed	Reyes-Reyes *et al.*, 2014[164]

Histopathology and biofluid screening

Tissue type	Details	Data processing method	Citations
Human breast	Introducing custom-made setup		Yeh *et al.*, 2014[59]
Mouse lung	Assessing discrete frequency imaging		Yeh and Bhargava, 2016[88]
Human cardiovascular	Distinction between myocardium and fibrosis	Bayesian classifier	Tiwari *et al.*, 2016[185]
Mouse jejunum	Identification of tissue types	*k*-Means clustering	Kröger *et al.*, 2014[87]
Mouse colon	Differentiation of ulcerative and infectious colitis	*k*-Means clustering	Kröger-Lui *et al.*, 2015[187]
Human breast	Assessing discrete frequency imaging		Bassan *et al.*, 2014[179]
Human prostate	Discrimination of normal and cancerous epithelium	Random forest algorithm	Pilling *et al.*, 2016[168]
Human blood serum	Discrimination of normal and cancerous samples	Peak centroid correlation	Hughes *et al.*, 2016[180]
Human liver	Distinction between hepatocytes and fibrosis	PCA-LDA	Sreedhar *et al.*, 2016[191]
Human colon	Identification of tissue types	*k*-Means clustering	Bird and Rowlette, 2017[192]

Bodily fluids

Analyte	Matrix	Spectroscopic technique	Type	QCL type	QCL operation mode	Citations
Glucose	Blood serum	Transmission	*In vitro*	DFB-QCL	Pulsed	Martin *et al.*, 2005[199]
	Blood serum	Transmission	*In vitro*	EC-QCL	Pulsed	Brandstetter and Lendl, 2012[84]
	Blood serum	Transmission	*In vitro*	EC-QCL	Pulsed	Brandstetter *et al.*, 2013[73]
	Blood plasma	Transmission	*In vitro*	EC-QCL	Pulsed	Brandstetter *et al.*, 2013[201]
	ISF	Fiber-based transmission	*In vivo* – invasive	FP-QCL	Pulsed	Vrančić *et al.*, 2014[206]
	Blood serum	Transmission	*In vitro*	EC-QCL	Pulsed	Liakat *et al.*, 2013[207]
	ISF	Backscattering	*In vivo* – non-invasive	EC-QCL	Pulsed	Liakat *et al.*, 2014[208]
	ISF	PAS	*In vivo* – non-invasive	DFB-QCL	Pulsed	von Lilienfeld-Toal *et al.*, 2005[211]
	ISF	PAS	*In vivo* – non-invasive	DFB-QCL	Pulsed	Pleitez *et al.*, 2012[212]
	ISF	PAS	*In vivo* – non-invasive	EC-QCL	Pulsed	Pleitez *et al.*, 2013[213]
	ISF	PAS	*In vivo* – non-invasive	EC-QCL	Pulsed	Pleitez *et al.*, 2013[214]
	ISF	PTD	*In vivo* – non-invasive	EC-QCL	Pulsed	Pleitez *et al.*, 2015[215]
	ISF	PTD	*In vivo* – non-invasive	EC-QCL	Pulsed	Hertzberg *et al.*, 2017[216]
	ISF	PAS/PTD	*In vivo* – non-invasive	EC-QCL	Pulsed	Bauer *et al.*, 2017[217]
	ISF	Reflectometry	*In vivo* – non-invasive	EC-QCL	Pulsed	Pleitez *et al.*, 2017[218]
	ISF	PAS	*In vitro*	EC-QCL	CW	Kottmann *et al.*, 2012[219]
	ISF	Fiber-based PAS	*In vivo* – non-invasive	EC-QCL	CW	Kottmann *et al.*, 2013[220]
	ISF	Fiber-based PAS	*In vivo* – non-invasive	EC-QCL	CW	Kottmann *et al.*, 2016[221]

Table 1 (*continued*)

Bodily fluids						
Analyte	Matrix	Spectroscopic technique	Type	QCL type	QCL operation mode	Citations
Cocaine	Saliva	Waveguide	*In vitro*	DFB-QCL	CW	Wägli *et al.*, 2013[224]
	Saliva	Waveguide	*In vitro*	DFB-QCL	CW	Jouy *et al.*, 2014[225]

DFB: distributed feedback, EC: external cavity, QCL: quantum cascade laser, AS: (direct) absorption spectroscopy, CE: cavity enhanced, OA-ICOS: off-axis integrated cavity output spectroscopy, WMS: wavelength modulation spectroscopy, FRS: faraday rotation spectroscopy, CRDS: cavity ring-down spectroscopy, QEPAS: quartz enhanced photoacoustic spectroscopy, ISF: interstitial fluid, PAS: photoacoustic spectroscopy, PTD: photothermal deflectometry.

ppmv to pptv range.[113] For selective mid-IR spectroscopic detection, this implicates that an analyte-specific absorption line needs to be identified which does not overlap with absorption bands of interfering matrix compounds that occur at much higher concentrations. In order to detect analytes at those low concentration ranges, diverse methods have been implemented to enhance the limits of conventional direct laser absorption spectroscopy (LAS). Among them, multipass absorption spectroscopy, cavity ring-down spectroscopy (CRDS), integrated cavity output spectroscopy (ICOS), as well as photoacoustic spectroscopy (PAS) and quartz-enhanced photoacoustic spectroscopy (QEPAS) have to be mentioned.[1,80,114]

Clinical breath analysis can be classified in two categories. One category marks the analysis of molecules that are endogenously produced due to normal or abnormal metabolic processes and thus may act as indicators (biomarkers) of specific diseases or metabolic disorders.[115,116] The concentration of these volatile organic compounds (VOC) depends on food intake, state of physical condition and general health as well as multiple environmental factors.[117] As some of these compounds may also be present in ambient air and may be consequently inhaled, strategies for the elimination or discrimination between exogenous and endogenous origin need to be devised.[118] The second category comprises the detection of isotopic labelled species such as carbon dioxide or nitrous oxide after administration and *in vivo* metabolism of ^{13}C or ^{15}N-labelled substrates. In this approach, there is no interference of exogenously present analyte, however, the applied analytical method needs to be capable of discriminating between naturally occurring and labelled gas species. Quantification of $^{13}CO_2$ or ^{15}NO allows for indirect *in vivo* determination of pharmacokinetics and the evaluation of specific enzyme activities.[119] There are numerous ^{13}C-labelled substrates that are used for study and diagnostics of diverse diseases and bodily malfunctions[112,113] Examples for common applications include the test on *Helicobacter pylori* infections based on a ^{13}C-labelled urea substrate, or a method testing the capacity of the human liver involving ^{13}C-caffeine.[120] ^{15}N-arginine is employed for metabolic studies of arginine metabolism in patients with asthma or pulmonary hypertension.[121,122]

Isotope ratio analysis is routinely performed by isotope-selective mass spectrometry combined with gas chromatography (GC-MS) and isotope ratio mass spectrometry (IRMS) that provides exceptional sensitivity but is also complex, bulky and expensive to acquire and maintain.[123] The development of non-dispersive isotope selective infrared spectrometry (NDIRS)[124] lead to a widespread applicability of ^{13}C-breath tests due to the lower cost and higher portability of the instruments, that require a sample volume of 500–1000 mL and provide equivalent results to IRMS.[119] Discrimination of $^{12}CO_2$ and $^{13}CO_2$ by IR spectroscopy is based on the isotopic wavenumber shift of the asymmetric stretching modes (ν_3, 2300–2400 cm^{-1} for $^{12}CO_2$, 2225–2335 cm^{-1} for $^{13}CO_2$) based on their difference in mass that results in almost complete separation of the absorption features. Due to the narrow tuning range of the DFB-QCL light sources, single rotational–vibrational lines of $^{12}CO_2$ and $^{13}CO_2$ need to be carefully selected. In this spectral region, several laser-based sensing approaches have been implemented,[125–127] before the first QCL-based setup has been realized for CO_2 isotope analysis by Weidmann *et al.*[128] It employed a Peltier-cooled DFB-QCL operated in pulsed mode, a dual multipass absorption cell and was optimized for mobile use. The first QCL-based setup particularly dedicated for determination of $^{12}CO_2/^{13}CO_2$ ratio in human breath was employed for testing the liver function.[129] Rubin *et al.* utilized a pulsed DFB-QCL with a balanced detection scheme. The flow-through arrangement enabled continuous real-time measurements with sensitivity in the ppbv range by Lorentzian fitting of single rotational–vibrational lines. Kasyutich *et al.* applied a DFB-QCL in CW mode with balanced detection and achieved single point measurements at CO_2 concentration with LOD in the ppbv range after Voight fitting of the absorption peak areas.[130] Most recently, Wörle *et al.* introduced a device for CO_2 isotope analysis in mice breath based on an EC-QCL light source coupled to a hollow core waveguide (HWG).[131] A HWG is a light pipe with the inner surface coated with highly reflective layer that acts both as optical waveguide and gas cell that enables sample volumes as low as approx. 100 μL. The application of a broadly tunable EC-QCL facilitated spectroscopic coverage of the entire ν_3 absorption features of $^{12}CO_2$ and $^{13}CO_2$. After multivariate data processing, comparable results to GC-MS could be obtained for the isotopic ratio.

For detection and discrimination of ^{14}NO and ^{15}NO, an approach based on Faraday rotation spectroscopy (FRS) has been presented.[132] Spectroscopic analysis of NO in the mid-IR region is performed by targeting fundamental rotational–vibrational absorption lines in the wavenumber range of 1800–1950 cm^{-1}. Although sensitive methods for NO analysis in breath are available (see below), the advantage of FRS is its exclusive selectivity to paramagnetic species such as NO, thus avoiding spectral

interference with ubiquitous diamagnetic species in breath samples such as H_2O and CO_2 that also absorb in the mid-IR region. In FRS, a magnetic field is applied to the sample cell containing paramagnetic species, along the propagation direction of the probe laser beam. Due to Zeeman splitting of the paramagnetic transitions, the sample exhibits magnetic circular birefringence *i.e.* a difference in refractive indices for left-handed and right-handed circularly polarized components. Hence, propagation of linearly polarized light through the sample causes rotation of its polarization axis which is proportional to the concentration of the analyte. The resulting small phase-shift between circularly polarized components is detected after an analyzer that is perpendicularly oriented with respect to the polarization of the incident light. In the developed setup, a DFB-QCL emitting near 1842 cm^{-1} is employed to target both the ^{14}NO and ^{15}NO absorption lines in combination with a TE-cooled MCT detector, enabling cryogen-free and portable operation. A magnetic field of 158 G is applied to the gas cell (effective path length: 45 cm) by an air core solenoid. For sensitive detection, a dual-modulation detection method has been devised, employing both magnetic field and laser wavelength modulation as depicted in Fig. 3A. Detection limits of 3.72 ppbv $Hz^{-1/2}$ for ^{14}NO and 0.53 ppbv $Hz^{-1/2}$ for ^{15}NO could be achieved. In preliminary tests, this system has been successfully applied for continuous breath analysis.[133] Furthermore, it has been used in a clinical setup for off-line analysis of nitrite/nitrate in urine after chemical conversion to NO.[134] Labelled and unlabelled NO metabolites were detected and quantified in urine samples collected before and after administration of ^{15}N-arginine (see Fig. 3B).

QCLs have been also employed for analysis of biomarkers in breath. Breath gas concentration of biomarkers can be associated with respective blood concentrations and thus to related metabolic processes. Among the numerous breath biomarkers,[113,115] several have been the target of spectroscopic analysis employing QCLs. Acetone is an attractive biomarker as it is the most abundant volatile compound endogenously released by the lungs. Reported concentrations for healthy individuals range from 0.39 to 1.09 ppm. Elevated levels of acetone in human breath have been related with type 1 diabetes.[135] Consequently, acetone analysis in breath poses an compelling alternative for screening of potential diabetes patients as opposed to invasive determination of blood glucose. Within the mid-IR range, acetone shows a broad absorbance feature between 1180 and 1250 cm^{-1} originating from the C–C stretching vibration.

In 2012, Ciaffoni *et al.* developed a spectrometer setup that combined a CW–DFB-QCL operated at ~8.2 μm (1216.5 cm^{-1}) with cavity-enhanced absorption spectroscopy.[136] After experimental removal of water vapor, similar acetone concentrations as with mass spectrometry were obtained with a LOD of 0.51 ppmv. Reyes-Reyes *et al.* employed a pulsed EC-QCL covering the spectroscopic region between 850 and 1250 cm^{-1} to perform direct absorption spectroscopy using a multipass gas cell with an optical path of approx. 55 m.[137] After computational removal of the water absorption lines, the acetone concentration was obtained by multiline fitting with a limit of detection of 0.15 ppmv.

Carbon monoxide is a gas that is both formed endogenously but also inhaled from the environment. In the metabolism, CO is generated during the catalytic breakdown of heme and most of the produced gas is exhaled resulting in a concentration of 1–3 ppmv CO in the breath of a healthy, non-smoking human.[138] As CO levels in the breath of smokers are approx. five times higher, screening of CO has been proposed to assess smoking status and behaviour.[139] Further, CO has been implicated as possible indicator of lung inflammation or oxidative stress. For CO analysis *via* IR spectroscopy, often an absorption line in the R-branch of the CO stretching absorption feature is chosen ranging between 2150 and 2220 cm^{-1}. Moeskops *et al.* reported CO measurements in breath employing a pulsed DFB-QCL using a multipass cell with a path length of 20 m.[140] Different spectrometer configurations (laser pulse length, balanced detection, amplitude modulation) were compared to achieve optimal sensitivity and selectivity and detection of minimum CO concentrations of 40 ppbv was experimentally shown. For real-time CO monitoring, a LOD of 175 ppbv was obtained at an integration time of 0.2 s and continuous measurements along several breaths were demonstrated. Pakmanesh *et al.* employed a CW–DFB-QCL to compare off-axis integrated cavity output spectroscopy (OA-ICOS) and wavelength modulation 2*f*/1*f* spectroscopy (WMS) for CO analysis in breath.[141] To minimize drifts of the

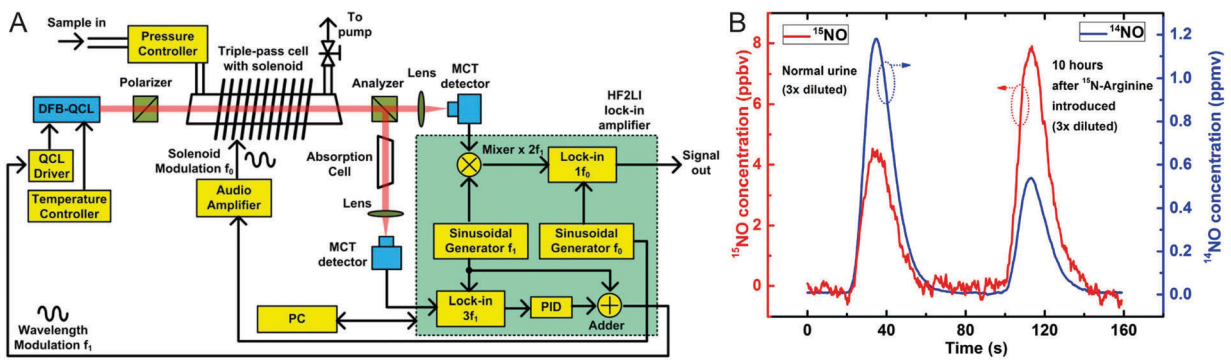

Fig. 3 (A) Schematic configuration of a FRS system. (B) Measurement of ^{15}NO (red) and ^{14}NO (blue) concentration after chemical conversion of nitrite/nitrate from patient's urine samples obtained before and after ^{15}N labeled arginine was introduced. Reproduced from ref. 132 with permission from Nature Publishing Group, copyright 2015.

laser wavelength, the QCL frequency was locked to a scanned absorption line in a reference cell. The WMS setup featuring a 20 cm absorption gas cell and lock-in detection shows similar performance as the OA-ICOS approach with an effective optical path of 160 m and a detector featuring a 400 times better detectivity. With both setups, a detection limit of 21 ppbv was reached at 1 s averaging time. More recently, Ghorbani *et al.* demonstrated simultaneous real-time measurements of exhaled CO and CO_2 utilizing a CW–EC-QCL with a MHF tuning range from 2080–2173 cm^{-1}.[142] Employing a circular multipass cell with an effective path length of 3.99 m and 2*f*-WMS curve fitting, detection limits of 9 ppbv and 650 ppmv could be achieved at 0.14 s spectrum acquisition time for CO and CO_2, respectively.

Ammonia in breath originates from metabolic breakdown of proteins. Exhaled ammonia concentrations of healthy individuals range from 0.25 to 2.9 ppm.[143] Increased levels of ammonia in breath has been associated with liver and kidney disorders, and *helicobacter pylori* infections.[144] For analysis of gas-phase ammonia, absorption lines near the ν_2 umbrella mode at 932.4 cm^{-1} are selected that do not overlap with adjacent absorption lines of interfering gas species. In 2006, Manne *et al.* developed a breath gas analyser based on pulsed cavity ring-down spectroscopy (CRDS) employing a DFB-QCL operating near 970 cm^{-1}.[145] At 20 s integration time, a sensitivity of 50 ppbv was demonstrated for analysis of human breath. It was shown that the ammonia level in breath increases after food intake. More recently, the same group compared inter- and intra-pulse techniques for ammonia detection employing a DFB-QCL and an astigmatic Herriot cell with 150 m path length.[146] Detection limits for breath ammonia were 3 ppbv at an integration time of less than 10 s and 4 ppbv at 5 s integration time for the inter- and intra-pulse technique, respectively. Tittel *et al.* presented an ammonia breath sensor based on quartz enhanced photoacoustic spectroscopy employing a CW–DFB-QCL, which was line-locked to an ammonia absorption line free from H_2O, CO_2 and methanol interferences, see Fig. 4A.[147–149] This configuration allowed for a minimum detectable ammonia concentration of 6 ppbv at an integration time of 1 s. Fig. 4B shows a typical breath ammonia profile obtained by this setup. The higher ammonia level in the first part reflects the concentration in the oral cavity, related to oral bacterial processes. After breath sampling is completed, remaining ammonia is removed from the system. This sensor platform has been tested on-site in an medical breath research center. Owen *et al.* developed an ammonia breath sensor based on a CW–DFB-QCL operated near 1103.44 cm^{-1} employing 2*f*/1*f* WMS detection.[150] The minimum detectable ammonia concentration was found to be 7 ppbv. In this study, ammonia levels of chronic kidney disease patients (1000 to 4500 ppbv) were found to be approx. ten times higher than of healthy individuals (100 to 350 ppbv).

Nitric oxide (NO) is an attractive gas species for analysis applications as it is relevant for atmospheric pollution monitoring and vehicle exhaust control. In human metabolism, NO is involved in numerous important functions related to immune reactions and neurotransmission.[151] The concentration of NO in breath of healthy individuals originating from the lower pathways ranges from 5 to 20 ppbv, NO concentration stemming from the nasal cavity varies between 40 to 200 ppbv.[152] Elevated levels of exhaled oral NO (20–80 ppbv) have been related to inflammatory respiratory disorders such as asthma. Currently, the analysis method for clinical NO measurements approved by the US Food and Drug Administration (FDA) is based on chemiluminescence after reaction of NO with ozone, featuring a LOD of <1 ppbv at an response time of 1 s.[153] Further employed techniques are based on electrochemistry and laser-based spectroscopy. There is a commercially available QCL-based gas sensor for NO and other gases that has been applied for determination of exhaled NO in clinical studies.[154] QCL-based sensors for exhaled NO detection have been developed based on absorption spectroscopy using a multipass cell[155–157] or a high finesse cavity for cavity enhanced,[155,158–163] as well as cavity ring-down[164] spectroscopy. McCurdy *et al.* reported an ICOS based spectrometer employing a CW–DFB-QCL operating at 1915 cm^{-1} capable of performing real-time measurements of NO and CO_2 in a single breath cycle.[161] The sensor employed a 50 cm long high-finesse optical

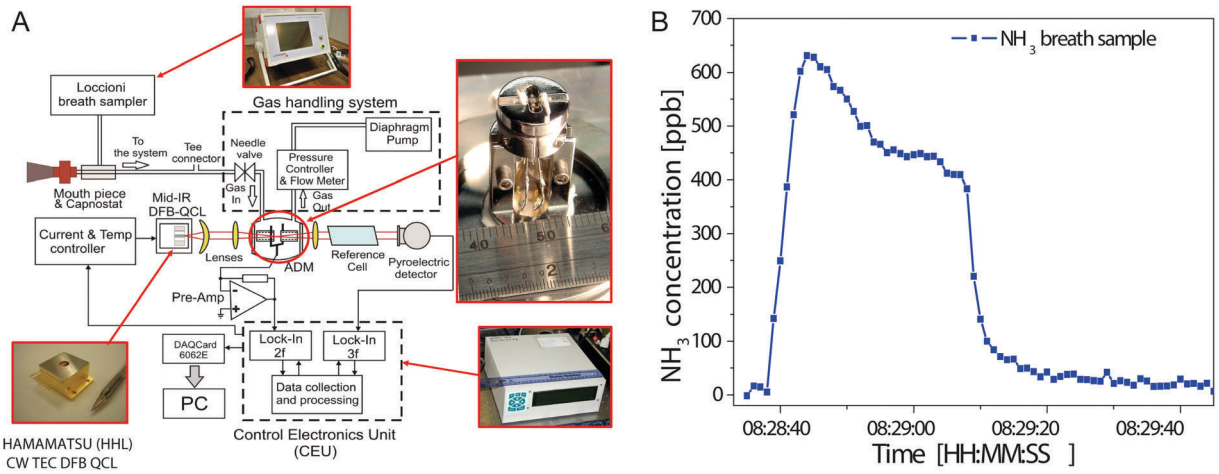

Fig. 4 (A) Block diagram of ammonia breath sensor architecture. (B) Time-resolved breath ammonia profile. Reproduced from ref. 147 with permission from SPIE Press, copyright 2011.

cavity that provides an effective path length of approx. 700 m. A LOD of 1.2 ppbv at 1 s integration time was achieved. Comparison of the data obtained from multiple breath measurements showed good agreement with a commercial chemiluminescence analyser. A NO sensor based on a CW–DFB-QCL operated between 1891 and 1908 cm^{-1} in combination with a multipass cell with an optical path length of 76 m was presented by Mandon *et al.*[157] By employing a wavelength modulation scheme this approach allowed a LOD of 0.5 ppbv at an integration time of 1 s. The results obtained by this sensor device were found to be in clinically acceptable agreement with a commercial chemiluminescence and electrochemical analyser. Most recently, a CW–EC-QCL cavity ring-down spectrometer has been reported for NO detection and was tested for breath analysis.[164] The EC-QCL was operated in mode-hop-free mode combined with a high-finesse optical cavity of 50 cm that provides an effective optical path of approx. 1.7 km. At an integration time of 13 s (*i.e.* 1200 ring-down decay signals), a LOD of 57 pptv could be achieved.

Apart from the described approaches focussing on detection of one single gas species, there have been attempts to perform multigas analysis in breath samples. Shorter *et al.* combined two commercially available QCL sensors in a custom-built instrument for multicomponent breath analysis.[154,165] The system comprises a breath sampling system for multiple exhalation flows and the associated pumping system together with two gas sensors employing a 75 m multipass cell and pulsed DFB-QCLs operating at 1900 cm^{-1} for NO and CO_2 and 2190 cm^{-1} for CO and N_2O analysis, respectively. The presence of NO and CO in breath have been identified as biomarkers of asthma and chronic obstructive pulmonary disease (COPD). Monitoring of CO_2 offers the additional value of determining dead space volume. For NO, a LOD of 0.9 ppbv was obtained at an integration time of 1 s. The sensor device allowed to collect real-time data at an acquisition rate of 10 Hz. Spectra of exhaled breath are shown in Fig. 5A and B along with the simultaneous measured data obtained from breath analysis in Fig. 5C. This setup was the first QCL-based system used for a clinical study of exhaled breath from patients with asthma and COPD.[154]

Reyes-Reyes *et al.* employed a pulsed EC-QCL operated between 830 and 1250 cm^{-1} in combination with a 55 m multipass transmission cell and a balanced detection scheme for multicomponent gas analysis.[166] Concentration determination was possible for molecules with a broad spectral profile such as acetone and ethanol but was impaired for species with sharp spectral features such as carbon dioxide. This setup was used in a clinical study of children with asthma and cystic fibrosis. Discrimination between healthy individuals and patients was conducted by chemometric analysis without concentration determination of the individual gas species.[167]

3.2. QCL-IR imaging for histopathology and biofluid screening

Over the last decade, there have been an increasing number of reports on employment of QCLs for imaging applications. Infrared microscopy offers the possibility to support clinical

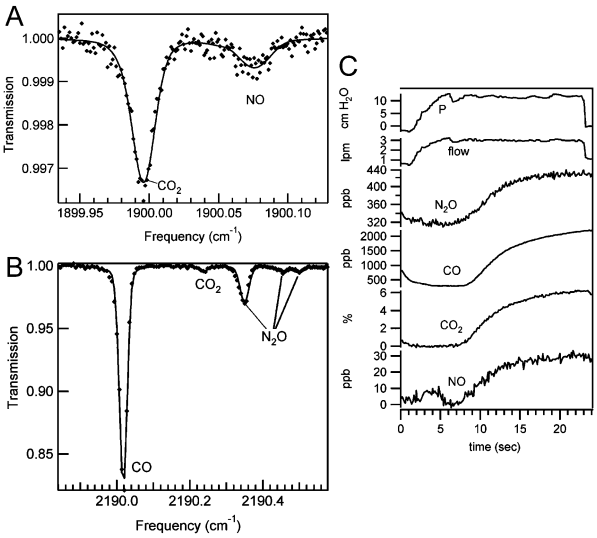

Fig. 5 (A) QCL-IR spectrum of 18.1 ppbv NO and 4.5% CO in exhaled breath. (B) QCL-IR spectrum of exhaled breath containing 2.2 ppmv CO and 417 ppbv NO. (C) Simultaneous exhaled breath data collected from a healthy male. Reproduced from ref. 165 with permission from IEEE, copyright 2010.

diagnostics in histopathology and biofluid screening. Traditionally, histopathology is based on identification of changes in morphology and architecture of potentially diseased tissue. Every biopsy tissue sample needs to be fixed, thin-sectioned and stained prior to individual microscopic examination. Currently, this approach is considered as the gold standard for identifying the manifestations of disease in tissue. However, the time-consuming procedure introduces significant delays between biopsy and diagnosis, and it has been shown that diagnosis based on tissue morphology and architecture is intrinsically subjective and leads to intra- and inter-observer error.[168,169] Due to the high information density of IR imaging, biological samples can be investigated without the need of endogenous labels, in a non-destructive manner and with little or no sample preparation.[170] In combination with advanced chemometric data evaluation, IR imaging can provide an approach for spectral histopathology that is based on objective interpretation of molecular changes in biopsy tissue. These biomolecular tissue transformations precede any morphological change, consequently diseases can be potentially early-detected in pre-malignant stages.[3] In cancer diagnostics, discrimination between normal and cancerous tissue by IR spectral imaging has been demonstrated with high sensitivity and specificity,[171] as well as determination of cancer grade[172] and stage.[173] Furthermore, studies have shown that tissue deemed normal by traditional histopathological methods was identified as abnormal by IR spectral imaging.[174,175] Progress in this field has been recently reviewed.[3,170,176–178]

In addition to the added value of the aforementioned specific properties of QCLs, within the specific application in IR microscopy, the concept of discrete frequency (DF) imaging can be realized by employing QCLs. In this approach, imaging data is only measured at a specific set of wavenumbers that provide all the relevant analytical information. This results in a significant drop in measuring time and reduction of data

volume that consequently decreases data handling time for subsequent chemometric analysis.[179,180] An experimental benefit from sequentially imaging single wavenumbers is the possibility to optimize the optical focus for each wavenumber of interest.[181] The higher flux of QCLs allows to employ uncooled bolometer detectors instead of cryogenic mercury cadmium telluride (MCT) single point detectors and focal plane arrays (FPA).[182] So far, for QCL-IR microscopy and imaging, EC-QCLs have exclusively been used as light source, but for DF imaging also the application of DFB-QCLs seems feasible. Most recently, it has also been demonstrated, that even with full spectra acquisition, a QCL-based imaging systems may have 150× faster acquisition times than FTIR microscopes at equivalent signal-to-noise level.[75] In 2014, the first commercial QCL-based IR imaging system became available (Spero, Daylight Solutions Inc., San Diego, CA, USA).

After early demonstrations of the feasibility of QCL-based IR microscopy,[183,184] particularly the Bhargava group focussed on development and characterisation of a custom-built setup[59,182] and subsequent application to biomedical and clinical questions.[59,88] Using their setup, Kole *et al.* discussed the implications of employing a spatially coherent light source for IR imaging and the resulting spectral differences.[182] Yeh *et al.* coupled a pulsed EC-QCL source containing four individual QCL chips (covering the combined tuning range of ~780 to 1900 cm^{-1}) to a FPA–MCT detector.[59] In this study, an unstained breast tissue was imaged in transmission mode by the QCL-FPA system and compared to FTIR imaging. A gain factor of 1100/*N* in acquisition time has been reported, where *N* constitutes the number of recorded wavenumbers. Subsequently, this setup was adapted for confocal reflection microscopy and equipped with a MCT detector.[88] Mouse lung tissue was DF-imaged at a data acquisition rate of 400 kHz, achieving RMS noise levels down to 0.34 mAU in 0.25 ms per pixel and wavelength. Tiwari *et al.* employed a recently announced commercial QCL-based IR imaging system (LaserDirect IR imaging system, Agilent, Santa Clara, CA, USA) for identification of infiltration and fibrosis in endomyocardial biopsy samples to asses transplant rejection.[185] Discrimination in DFIR images between two histopathological classes was obtained by a Bayesian classification algorithm trained on FTIR data as well as on DFIR data. The classifier developed on FTIR imaging data also sufficiently worked with high accuracy on DFIR imaging data, covering a relevant single spectral feature (Fig. 6). This may seem relevant for transferring already built classifiers based on FTIR data for use with DFIR data. It was reported that using this approach, pathologic recognition was at least 16 times faster than with an FTIR imaging system.

Development of a custom-built setup has also been accomplished by the Petrich group. Kröger *et al.* compiled a transmission mode microscopy setup comprising a CW–MHF–EC-QCL with a tuning range from 1030 to 1090 cm^{-1} and a microbolometer FPA.[87,186] The detector signals were filtered by a lock-in amplifier and wavenumber calibration was achieved by simultaneously measuring the transmission spectrum of ethanol vapour. The performance of this setup on imaging an unstained thin section of mouse jejunum was compared to FTIR mapping and imaging.

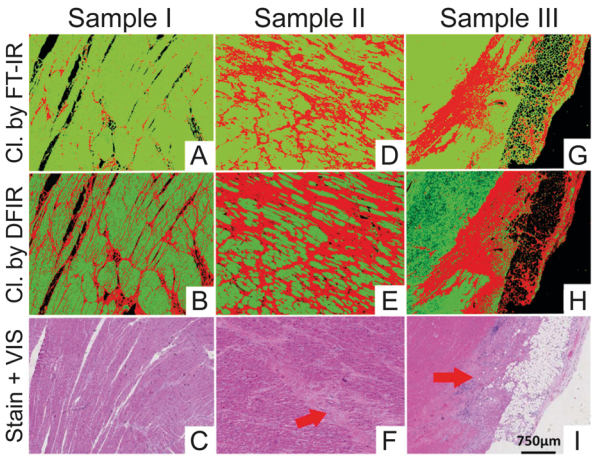

Fig. 6 Classification results shown for DFIR images of three different samples. (A, D and G) Classifier developed on FT-IR data. (B, E and H) Classifier developed on DFIR data. Red regions in all the IR colored images are fibrosis. Corresponding H&E images are shown in (C, F and I). Red arrows indicate the regions identified by the pathologist as fibrosis. Reproduced from ref. 185 with permission from American Chemical Society, copyright 2016.

Despite the small spectral region covered by the QCL-based setup, similar tissue morphology could be visualized by application of *k*-means clustering. The gain in acquisition time normalized to measured area and spectral range was estimated to be approx. three orders of magnitude. The developed setup, extended by a pulsed EC-QCL operating between 1160 and 1320 cm^{-1}, was employed for investigation of unstained thin sections of mouse colon mucosa.[187] After training a random decision forest classifier on the basis of *k*-means clustering, goblet cells could be successfully identified in further thin sections. Acquisition of the hyperspectral image (in scan mode) and data analysis was reported to take 7.5 minutes. Subsequently, the setup was used to demonstrate real-time imaging of a living microorganism, achieving a frame rate of 50 Hz at a discrete wavenumber.[188,189]

The Gardner group focussed on spectral histopathology employing commercially available QCL-IR microscopes. Bassan *et al.* employed a Spero QCL-IR microscope (Daylight Solutions Inc., San Diego, CA, USA) equipped with a microbolometer FPA for imaging a breast tissue micro array (TMA) with approx. 200 cores.[179] At a single wavenumber, the area of 20 × 24 mm^2 was imaged at a measurement time of 9 min. Subsequently, human prostate tissue samples were examined using DFIR imaging.[168] The performance of a classifier based on a random forest algorithm for discrimination between normal and cancerous epithelium was tested at incorporating differing numbers of wavenumbers. Evaluation of images acquired in the spectra range 1000–1800 cm^{-1} (160 wavenumbers) using a GINI importance plot resulted in a significant drop in importance after the top 20 spectra. Analysis by receiver operator curves (ROC) showed only marginal effect on the classifier performance after reduction of the included wavenumbers between 25 and 16, considerably reducing the data acquisition time for each sample. However, it was noted that for acquiring a robust model for clinical use, a larger patient population needs to be involved to consider

biochemical variability between patients, potentially leading to a larger number of key biomarkers.

In the Baker group, QCL-based IR microscopy was not only employed for tissue analysis but also for investigations of biofluids.[190] Hughes *et al.* applied QCL-IR microscopy for human blood serum based screening of cancer.[180] The samples were imaged using different discrete frequency ranges and the resulting dataset was subsequently assessed in terms of spectral reproducibility, as depicted in Fig. 7A. Cancer and non-cancer samples were distinguished by evaluation of centroid positions of amide I and amide II bands. It has been demonstrated, that the diagnostic potential for discrimination was preserved even when fewer wavenumbers were acquired, accompanied by considerable reduction in acquisition time (image of one serum spot: 11.3 minutes for 199 data points *vs.* 1 minute for 9 data points), see Fig. 7A and D. Discrete frequency spectra depicting the amide I and amide II region acquired with a different number of data points are shown in Fig. 7B and E. Distinction between cancerous and non-cancerous patient samples has been performed by calculation of the centroid positions of amide I and amide II bands (Fig. 7C and F). In a proof-of-concept experiment involving 40 unique dried liquid biopsies from brain, breast, lung and skin cancer patients, classification against 10 non-cancer controls could be achieved with accuracies of up to 90%.

Furthermore, Sreedhar *et al.* employed QCL-IR imaging to detect chemical modifications in liver fibrosis due to diabetes and disease.[191] A commercial microscope was employed to study TMAs of liver tissue biopsies. By application of principal component analysis-linear discriminant analysis (PCA-LDA) on full spectra (900–1800 cm^{-1}) hepatocytes and fibrosis could be successfully distinguished. Furthermore, discrimination between diabetic and nondiabetic patients was obtained in regions of fibrosis but not in hepatocyte due to high intra-class variance.

More recently, Bird *et al.* used QCL-IR imaging to discriminate major tissue structures in colorectal biopsy samples.[192] IR images comprising 10 discrete frequencies were acquired employing a commercial microscope. Different colon tissue classes (protein, collagen, mucin) could be differentiated after generating spectral descriptors. Alternatively, *k*-means clustering was applied to full band spectral datasets (900–1800 cm^{-1}, data interval: 4 cm^{-1}) to achieve discrimination between tissue structures.

3.3. Analysis of bodily fluids

The high available laser power facilitated the utilization of QCLs for clinical and biomedical applications on biofluids. To date, QCLs have been predominantly applied for glucose monitoring in blood (*in vitro*) and interstitial fluid in skin (*in vivo*) but also for drug testing in saliva. The limiting factor for biofluid analysis by mid-IR spectroscopy is the continuum absorbance of water below 2000 cm^{-1}.[193] For transmission measurements using FTIR, this implicates confinement to low path length up to 50 μm in the carbohydrate region (950–1250 cm^{-1}) or even below 10 μm in the protein region (1500–1700 cm^{-1}),[63] accompanied with considerable impairment of robustness during the measurement. Due to the high emission power of QCLs, the path length could be considerably increased.

The majority of reports about applications of QCLs for biofluid analysis focused on glucose analysis. This is an intensively researched field, as monitoring of blood glucose is an essential

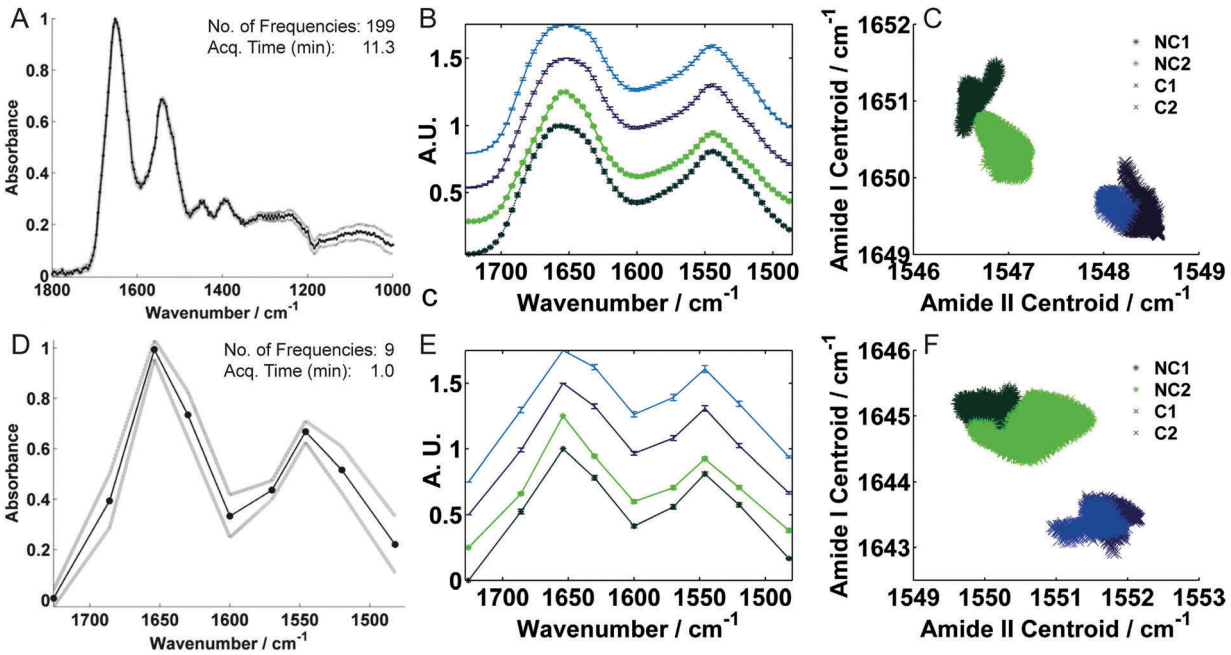

Fig. 7 QCL-IR microscopy spectra of dried human serum spots recorded with (A) 199 and (D) 9 discrete frequencies using different frequency ranges. (B and E) Mean representative spectra for non-cancer (NC, green) and brain cancer (C, blue) patient samples. (C and F) Corresponding amide I and II peak centroid correlation plots for full and sparse frequency data collection modes, respectively. Reproduced from ref. 180 with permission from Nature Publishing Group, copyright 2016.

part of diabetic management. Normal glucose levels in blood are in the range of 70–145 mg dL^{-1} (1 mg dL^{-1} = 10 ppm) with pathophysiological levels ranging between 35 and 540 mg dL^{-1}.[194] Currently, the most widespread method for self-monitoring is based on electrochemical biosensing after an enzymatic reaction. This procedure is considered as uncomfortable because it requires periodic (*i.e.* more than four times per day) invasive extraction of a drop of blood and costly because every measurement requires a new test strip. Throughout the last years, there has been intensive research to establish non-invasive techniques for continuous glucose monitoring.[194–198] In these approaches, blood is substituted by other fluids that contain glucose such as saliva, urine, tears or interstitial fluid (ISF) that is monitored through the skin. Among the spectroscopic techniques for non-invasive testing, the near-IR region has been frequently used due to the presence of glucose overtone bands in combination with low water absorption, which allows large penetration depth of the light into skin. However, in this region the spectral features of glucose strongly overlap with amide bands, thus quantification is challenging. Despite the higher water absorption and resulting lower penetration depth in skin, application of mid-IR spectroscopy proves to be promising, because the spectral features of glucose are inherently highly specific and consequently selective even in a complex matrix such as whole blood or interstitial fluid. Glucose gives a highly characteristic spectral signature between 950 and 1200 cm^{-1} attributed to C–O–H stretching and bending vibrational modes. Thus, no preceding reactions are needed to ensure selectivity of the analysis and reagent-free monitoring is feasible. Employing QCLs, glucose has been monitored *in vitro* in blood plasma and serum by transmission measurements and *in vivo* employing backscattering as well as photoacoustic and photothermal spectroscopy. The first successful glucose measurement in human serum was reported by Martin *et al.* in 2005.[199] Two pulsed DFB-QCLs where combined with a cryogenically-cooled MCT detector. The glucose absorption at 1036 cm^{-1} and background at 1194 cm^{-1} were consecutively measured in a 26.4 μm transmission cell, thereby achieving a standard error of 24.7 mg dL^{-1}.

With the emergence of EC-QCLs, the Lendl group focused on transmission measurements in blood serum and plasma. Brandstetter *et al.* employed a pulsed EC-QCL operated in scan mode between 1030 and 1230 cm^{-1} with a 130 μm transmission flow cell in combination with a TE-cooled MCT detector.[84,200] Employing partial least squares (PLS) regression analysis, a standard error of 2.2 mg dL^{-1} was reported for aqueous glucose standards in the physiological concentration range and the feasibility of measurements in blood serum samples was demonstrated. In subsequent works, the advantage of broadly tunable EC-QCLs was exploited by combination with multivariate data analysis to perform multi-component analysis.[73] The same setup was used for quantification of glucose, lactate and triglycerides in blood serum of 42 healthy donors by using PLS analysis. At a path length of 135 μm, glucose was determined with a prediction error of 6.9 mg dL^{-1}. The approach was further refined and presented as a point-of-care system for simultaneous quantification of up to eight blood parameters, including carbohydrates, lipids, proteins and urea in blood plasma of critically ill patients employing PLS analysis.[201] When using a path length of 165 μm, glucose was determined with a cross-validation error of 12.2 mg dL^{-1}. All measured data were within the clinically relevant limits of the Clarke error grid analysis for assessing the quality of glucose measurements.

Apart from the conventional transmission flow cell approach, the Petrich group established a fiber-based system with a small transmission gap, where the liquid sample is introduced. In 2006, Lambrecht *et al.* used this approach in combination with a FP-QCL for coupling into silver-halide fibers that were separated by a transmission gap of 20–100 μm.[202] Employing a pyroelectric detector, a sensitivity of 10 mg L^{-1} was obtained. After multiple refinement steps of the method,[203–205] Vrančić *et al.* presented a minimally invasive fiber-based sensor for continuous *in vivo* glucose monitoring.[206] Here, a pulsed, non-tunable laser operated at 1030 cm^{-1} was used with a pyroelectric detector. The silver halide fiber with a 20 μm gap was implanted in a rat's neck and changes of the glucose level were continuously monitored in the ISF after injections of glucose or insulin. The data obtained with this sensor was compared with a commercial blood glucose meter and an overall standard deviation of 17.5% was achieved. Assessment by the Clarke error grid indicated acceptable results from a medical standpoint.

The Gmachl group developed a non-invasive *in vivo* glucose sensing method based on detection of backscattered light from the skin. Initially, Liakat *et al.* reported on *in vitro* transmission measurements at 100 μm path length employing a pulsed EC-QCL laser tunable between 1000 and 1200 cm^{-1} coupled with a cryogenically-cooled MCT detector.[207] Quantification of glucose at relevant concentration ranges (1–400 mg dL^{-1}) in aqueous and serum solutions could be achieved by employing PLS modelling. The QCL data were compared with FTIR spectroscopy and clinically accurate measurements were obtained with respect to Clarke error grid analysis. More recently, a technique for *in vivo* glucose sensing based on backscattering spectroscopy was presented.[208] A pulsed EC-QCL tunable between 1000 and 1200 cm^{-1} was focused into a hollow-core fiber in order to deliver the light to the region of the human palm between thumb and index finger. The backscattered light was collected by a bundle of six fibers circularly arranged around the delivery fiber and detected by a cryogenically-cooled MCT detector. Glucose sensing in the dermal ISF was performed on three healthy humans and 84% of the obtained results lay within the clinically accurate regime of the Clarke grid for glucose concentrations between 75 and 160 mg dL^{-1}.

The Mäntele group pioneered the application of photoacoustic (PA) and photothermal deflection (PTD) spectroscopy in combination with QCLs for non-invasive glucose monitoring. When using these techniques, the sample is irradiated by a pulsed or modulated light source. Thermal relaxation after vibrational excitation generates a local temperature rise at the site of absorption that propagates as a periodic heat wave to the surface. Concurrently, a sound wave is generated by heat-induced expansion. Photothermal spectroscopy aims at measuring the heat wave, whereas in photoacoustic spectroscopy the sound wave is detected. A distinctive characteristic of these approaches

is the direct scaling of the signal with incident intensity and the absorption coefficient of the sample.[209,210] For non-invasive measurements, the measuring cell can be put in direct contact with different regions of the skin. The penetration depth of mid-IR light into skin is approx. 50–100 μm. Since blood vessels cannot be reached, PAS and PTD aim at measuring the glucose concentration in ISF that correlates with blood glucose levels with a time delay of roughly 10 minutes.

The first PAS application with QCLs as source of mid-IR radiation was reported by von Lilienfeld-Toal *et al.* in 2005.[211] The setup consisted of two single-mode QCLs emitting at 1080 cm^{-1} (for detecting glucose absorption) and 1066 cm^{-1} (for detecting background absorption). A twin measuring chamber was employed for simultaneously detecting the laser induced PA signal and the background noise. Overall, the results show poor correlation with blood glucose levels but demonstrate the feasibility of the method. Subsequently, the results were improved by extending the setup with an additional QCL for detecting glucose absorption.[212] Based on these results demonstrating the benefits of multi-wavelength detection, in a succeeding iteration of the setup, a pulsed EC-QCL tunable between 1000 and 1220 cm^{-1} was employed as a light source for PA measurements as depicted in Fig. 8A.[213,214] The PA cell was designed to operate in the ultrasound region at approx. 50 kHz, agreeing with QCL repetition rates, to reduce acoustic noise upon *in vivo* measurements. PLS analysis was employed to predict glucose levels in the *Stratum corneum* layer with a mean prediction error of 15 mg dL^{-1} in the range of 50–300 mg dL^{-1}. Results of PA measurements at the hypothenar of the hand throughout an oral glucose tolerance test of a healthy individual and a diabetes patient show high congruence with results from an enzymatic blood test without significant delay (<10 min). More recently, Pleitez *et al.* introduced an approach based on photothermal deflectometry enhanced by total internal reflection (TIR-PTD) spectroscopy for *in vivo* glucose measurements.[215] In this setup (Fig. 8D), a pulsed EC-QCL tunable between 1000 and 1220 cm^{-1} is employed as a pump source and is directed perpendicular into the truncated base of an internal reflection element (IRE). Modulation of the pump beam and sample absorption leads to a periodic increase of the local temperature near the IRE/sample interface, creating a thermal lens within the IRE that deflects the VIS probe beam, detected by a position sensitive diode. This technique enables to reach deeper skin layers compared to conventional attenuated total reflection (ATR) IR techniques. By application of PCA and PLS, glucose levels could be quantified with a prediction error of 9 mg dL^{-1} for

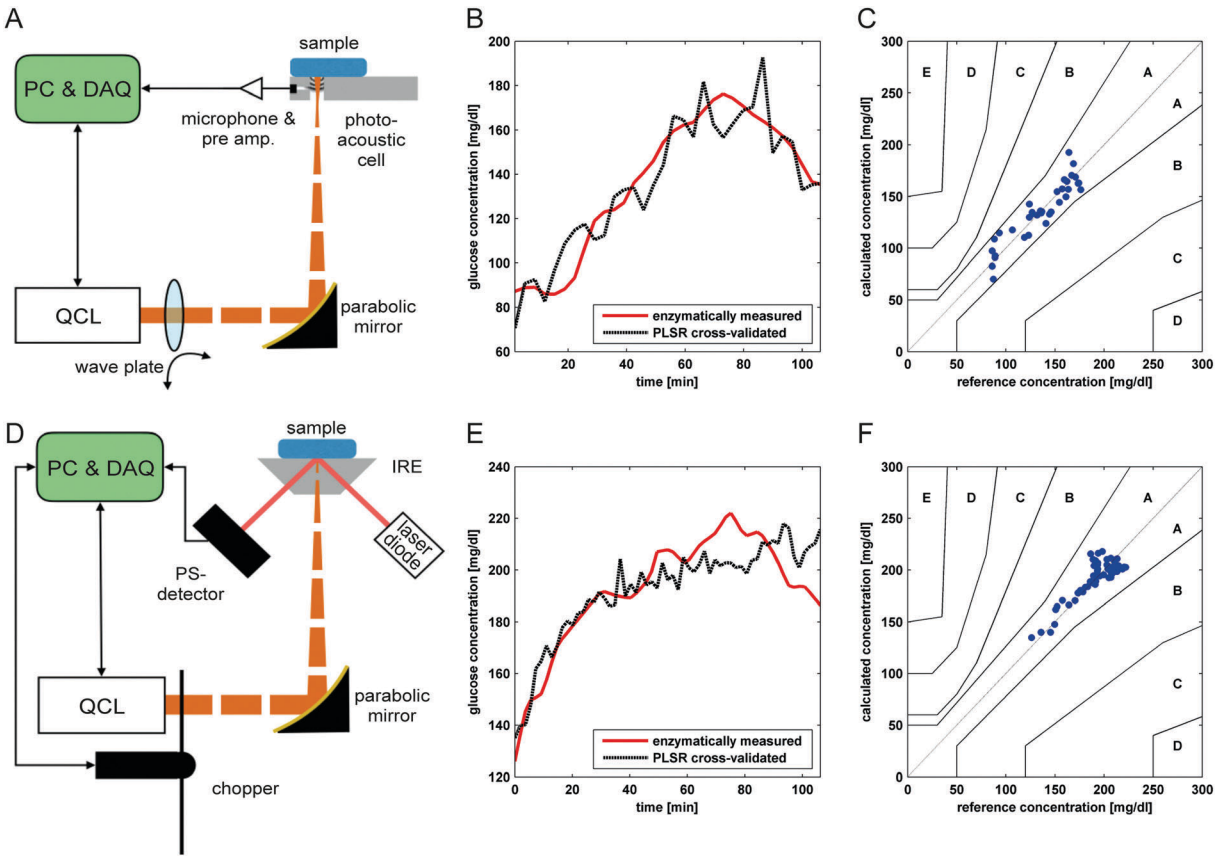

Fig. 8 Schematic drawings of the (A) photoacoustic and (D) photothermal setup. Non-invasively measured skin glucose concentrations calculated from PLSR cross-validation with skin spectra recorded by (B) photoacoustic detection on the index finger and (E) photothermal detection on the thumb of a volunteer *vs.* reference blood glucose. Consensus error grid representation of the non-invasive measurements recorded by (C) photoacoustic and (F) photothermal detection. Reproduced from ref. 217 with permission from Wiley-VCH, copyright 2017.

in vivo measurements at the hypothenar of the hand. Results obtained by TIR-PTD agreed well with a commercial blood glucometer for *in vivo* measurements of a diabetic patient after administration of insulin. Subsequently, this technique was applied to measure depth-dependent IR spectra of human skin by modulation of the pump beam frequency and thus the thermal diffusion length.[216] With regard to glucose measurements, it has been shown that depth profiling of the human skin can be used to improve quantification result by accounting for individual skin properties and day-to-day variations. Employing PLS, glucose levels could be quantified with a cross validation error of 24 mg dL^{-1} for *in vivo* measurements at the hypothenar of the hand. Bauer *et al.* contrasted results of non-invasive glucose monitoring performed by photoacoustic and photothermal skin measurements and reported lower cross validation errors for the photothermal method.[217] The results were well comparable to reference measurements (Fig. 8B and E) and lay within the clinically relevant range as revealed by consensus error grid analysis (Fig. 8D and F). Most recently, the results of photoacoustic and photothermal spectroscopy were compared with data obtained by IR light diffusely reflected from skin.[218] It was concluded that the shallow skin layers accessible by back-scattered IR light merely contains glucose at concentrations only weakly related to blood glucose levels.

Also the Sigrist group reported on developing a PAS system for non-invasive glucose monitoring. Kottmann *et al.* employed a CW–EC-QCL operated between 1034 and 1080 cm^{-1} with a mechanical chopper.[219] When measuring skin samples pretreated with glucose solution, a LOD of 100 mg dL^{-1} (SNR = 1) could be achieved. The same author reported on a silver halide fiber-based system employing a matching conically-shaped PA cell.[220] *In vitro* measurements of aqueous glucose solution yielded a LOD of 57 mg dL^{-1} (SNR = 1). Qualitative measurements of human skin were shown to demonstrate the potential of the setup. Subsequently, a PAS setup was presented employing two EC-QCLs at fixed emission wavelengths of 1080 and 1180 cm^{-1}.[221] An oral glucose tolerance test was performed with a healthy volunteer. Without applying chemometric methods, the computed signal ratio of the two wavelengths reasonably follows glucose levels that were simultaneously determined by a commercial glucometer.

Apart from the different approaches for quantification of glucose in blood and in the interstitial fluid of the epidermis, there have been efforts to detect cocaine in saliva based on QCL-IR spectroscopy. Saliva sampling is less invasive than blood testing and does not require medically trained staff. The aim is to develop a portable cocaine sensor for clinical and on-roadside drug testing. Currently, the results of immunoassay screening tools need to be confirmed by a subsequent blood test based on liquid chromatography combined with mass spectroscopy, involving complex sample preparation and bulky equipment. The legal limit for cocaine in saliva in most countries is 20 ng mL^{-1}, whereas the level can get as high as 500 μg mL^{-1} from a single 40 mg dose of cocaine.[222] Chang *et al.* coupled a single mode CW–DFB-QCL operated at 1724 cm^{-1} with a Si/Ge waveguide to detect carbonyl vibrations of cocaine. The sample solution was applied *via* a microfluidic system.[223] Due to the high absorption of the aqueous sample matrix, on-line microfluidic liquid–liquid extraction of the analyte from saliva to tetrachloroethylene was devised.[224] Employing this setup, real-time measurements of saliva samples spiked with cocaine were performed demonstrating a detection limit of 100 μg mL^{-1}.[225]

4. Conclusions and outlook

The surveyed work shows an impressive collection of QCL-based applications in biomedical spectroscopy. Particularly the work on breath analysis benefits from the long-lasting experience of developing advanced QCL-based detection schemes for trace gas analysis. In contrast, current implementations of QCLs for biomedical analysis of liquids seem rather limited to the quantification of glucose in blood, but recent advancements in protein analysis[65,74] promise near-term extension to further applications, *e.g.* milk analysis.[226] Regarding QCL-IR imaging, the availability of commercially obtainable QCL-based microscopes will further expand the field of applications.

Apart from the technologies already adopted for biomedical sensing applications, there is ongoing progress in QCL engineering that may affect the design of upcoming sensing strategies. QCL-based mid-IR frequency combs[99] for dual comb spectroscopy[101] have been proposed for breath analysis[227] due to their high spectral resolution and fast response times, but with recently presented bandwidths of up to 150 cm^{-1}, this approach seems also feasible for measurements of liquid-state biomedical samples. Since spectral tuning is accomplished without moving parts, fluctuations in the emission spectrum originating from mode-hops[74,83] during scanning of EC-QCLs can be avoided. The same advantage is delivered by Vernier Effect based distributed Bragg reflectors (DBR)-QCL[228,229] and DFB-QCL arrays.[47] The latter have already been successfully employed for hyperspectral imaging[230] and are well suited for portable use.[231]

Quantum heterostructures can also be applied for detection purposes in the form of quantum cascade detectors (QCD).[232] QCLs and QCDs have already been integrated and measurements of gaseous[233,234] and liquid[235] samples have been demonstrated. This technology may have important implications for development of clinical devices, especially in regard to their miniaturization and integration to lab-on-a-chip sensors.

An alternative to conventional IR microscopy pose IR nanoscopic techniques such as AFM-IR (atomic force microscopy-based IR) spectroscopy[236] and scattering scanning near field optical microscopy (s-SNOM),[237] which are near-field detection techniques that allow spatial resolution on the nanometer scale. For both methods, QCLs are routinely employed as light sources. In AFM-IR spectroscopy, QCLs are preferably used because they offer high versatility in pulsed operation. The sub-diffraction limited spatial resolution of IR nanoscopy is particularly attractive for cell studies. AFM-IR spectroscopy was already employed for analysis of cancer[238] and single bacteria cells[239] and s-SNOM was applied for studies of blood cells[240] and viruses.[241] Although AFM-IR (nanoIR2, Anasys Instruments;

Vista-IR, Molecular Vista) and s-SNOM (nanoIR2-s, Anasys Instruments; neaSNOM, Neaspec) instruments are commercially available, application of these techniques will most probably be confined to the academic medical field and not be introduced to routine diagnostics.

This review summarizes the extensive technological advances in biomedical sensing applications involving QCLs and illustrates that the road is paved for their further use in a clinical context. However, the next step, being the transition from technical report to application in clinical trials and routine work is still in its infancy. To achieve this, different stakeholders (researchers, clinicians, and instrument manufacturers) need to cooperate. An important step is to overcome the nomenclature of the own scientific field and establish a common language. For example, spectroscopic and chemometric achievements can be expressed in terms of clinically relevant metrics such as sensitivity, specificity, ROC, AUC among others.[242,243] Notably, Clarke's error grid has been readily adopted as quality reference in most of the reviewed papers involving glucose quantification in blood.

Large scale trials are required to profoundly assess the future and eventually relevance of QCL-based spectroscopy in a clinical setting. In this regard, a robust device design is imperative that allows safe, low maintenance and durable operation, so that a user with little training can collect repeatable data. With a small footprint and often no need for cryogenically-cooled detectors, QCL-based instruments fulfil the fundamental requirements. These clinical trials will provide data about accuracy and validity of the methods and its efficacy within the clinical environment. Validated information about how accurately a new instrument can diagnose disease or perform treatment monitoring will ultimately be the basis for acceptance in the medical community.[244]

Finally, the herein presented and future developed spectroscopic methods based on QCLs need to actively demonstrate that they provide an added value over established, well documented, FDA-approved and cost efficient gold standards currently used in clinical diagnostics.

Conflicts of interest

There are no conflicts of interest to declare.

Acknowledgements

The authors thank Harald Moser for figure work. Financial support was provided by the Austrian research funding association (FFG) under the scope of the COMET programme within the research project ''Industrial Methods for Process Analytical Chemistry – From Measurement Technologies to Information Systems (imPACts)'' (www.k-pac.at, contract #843546) and by the strategic economic and research program ''Innovative Upper Austria 2020'' of the province of Upper Austria. The authors acknowledge the TU Wien University Library for financial support through its Open Access Funding Program.

Notes and references

1 F. K. Tittel and R. Lewicki, in *Semiconductor Lasers: Fundamentals and Applications*, ed. A. Baranov and E. Tournie, Woodhead Publ Ltd, Cambridge, 2013, vol. 33, pp. 579–629.
2 D. Perez-Guaita, S. Garrigues and M. de la and Guardia, *TrAC, Trends Anal. Chem.*, 2014, **62**, 93–105.
3 C. Kendall, M. Isabelle, F. Bazant-Hegemark, J. Hutchings, L. Orr and J. Babrah, *et al.*, *Analyst*, 2009, **134**, 1029–1045.
4 A. A. Bunaciu, H. Y. Aboul-Enein and S. Fleschin, *Appl. Spectrosc. Rev.*, 2015, **50**, 176–191.
5 A. A. Bunaciu, Ş. Fleschin, V. D. Hoang and H. Y. Aboul-Enein, *Crit. Rev. Anal. Chem.*, 2017, **47**, 67–75.
6 C. Petibois and B. Desbat, *Trends Biotechnol.*, 2010, **28**, 495–500.
7 R. A. Shaw, S. Low-Ying, M. Leroux and H. H. Mantsch, *Clin. Chem.*, 2000, **46**, 1493–1495.
8 K. Z. Liu, R. A. Shaw, A. Man, T. C. Dembinski and H. H. Mantsch, *Clin. Chem.*, 2002, **48**, 499–506.
9 M. J. Baker, J. Trevisan, P. Bassan, R. Bhargava, H. J. Butler and K. M. Dorling, *et al.*, *Nat. Protoc.*, 2014, **9**, 1771–1791.
10 C. I. L. Justino, T. A. Rocha-Santos and A. C. Duarte, *TrAC, Trends Anal. Chem.*, 2010, **29**, 1172–1183.
11 A. E. Siegman, *Lasers*, University Science Books, Mill Valley, California, USA, 1986.
12 Y. Yao, A. J. Hoffman and C. F. Gmachl, *Nat. Photonics*, 2012, **6**, 432–439.
13 F. Capasso, *Opt. Eng.*, 2010, **49**, 111102.
14 R. F. Curl, F. Capasso, C. Gmachl, A. A. Kosterev, B. McManus and R. Lewicki, *et al.*, *Chem. Phys. Lett.*, 2010, **487**, 1–18.
15 J. Faist, *Quantum cascade lasers*, Oxford University Press, Oxford, UK, 1st edn, 2013.
16 J. Faist, F. Capasso, D. L. Sivco, A. L. Hutchinson, C. Sirtori and A. Y. Cho, *Infrared Phys. Technol.*, 1995, **36**, 99–103.
17 F. Capasso, C. Gmachl, D. L. Sivco and A. Y. Cho, *Phys. Today*, 2002, **55**, 34–40.
18 R. F. Kazarinov and R. A. Suris, *Sov. Phys. Semicond.*, 1971, **5**, 707–709.
19 J. Faist, F. Capasso, D. L. Sivco, C. Sirtori, A. L. Hutchinson and A. Y. Cho, *Science*, 1994, **264**, 553–556.
20 C. Gmachl, D. L. Sivco, R. Colombelli, F. Capasso and A. Y. Cho, *Nature*, 2002, **415**, 883–887.
21 A. Hugi, R. Maulini and J. Faist, *Semicond. Sci. Technol.*, 2010, **25**, 083001.
22 B. Meng and Q. J. Wang, *J. Opt.*, 2015, **17**, 023001.
23 T. Kruczek, K. A. Fedorova, G. S. Sokolovskii, R. Teissier, A. N. Baranov and E. U. Rafailov, *Appl. Phys. Lett.*, 2013, **102**, 011124.
24 K. Ohtani, M. Beck, M. J. Suess, J. Faist, A. M. Andrews and T. Zederbauer, *et al.*, *ACS Photonics*, 2016, **3**, 2280–2284.
25 M. Razeghi, N. Bandyopadhyay, Y. B. Bai, Q. Y. Lu and S. Slivken, *Opt. Mater. Express*, 2013, **3**, 1872–1884.
26 M. S. Vitiello, G. Scalari, B. Williams and P. De Natale, *Opt. Express*, 2015, **23**, 5167–5182.
27 W. Ackermann, G. Asova, V. Ayvazyan, A. Azima, N. Baboi and J. Bahr, *et al.*, *Nat. Photonics*, 2007, **1**, 336–342.

28 J. Faist, M. Beck, T. Aellen and E. Gini, *Appl. Phys. Lett.*, 2001, **78**, 147–149.
29 C. Gmachl, F. Capasso, D. L. Sivco and A. Y. Cho, *Rep. Prog. Phys.*, 2001, **64**, 1533–1601.
30 R. Maulini, M. Beck, J. Faist and E. Gini, *Appl. Phys. Lett.*, 2004, **84**, 1659–1661.
31 A. Lambrecht, M. Pfeifer, W. Konz, J. Herbst and F. Axtmann, *Analyst*, 2014, **139**, 2070–2078.
32 S. Bartalini, S. Borri, P. C. Pastor, I. Galli, G. Giusfredi and D. Mazzotti, *et al.*, *Proc. SPIE*, 2011, **7945**, 794505.
33 J. S. Li, W. Chen and H. Fischer, *Appl. Spectrosc. Rev.*, 2013, **48**, 523–559.
34 A. Gordon, C. Y. Wang, L. Diehl, F. X. Kartner, A. Belyanin and D. Bour, *et al.*, *Phys. Rev. A: At., Mol., Opt. Phys.*, 2008, **77**, 053804.
35 C. Y. Wang, L. Diehl, A. Gordon, C. Jirauschek, F. X. Kartner and A. Belyanin, *et al.*, *Phys. Rev. A: At., Mol., Opt. Phys.*, 2007, **75**, 031802.
36 B. Lendl, J. Frank, R. Schindler, A. Muller, M. Beck and J. Faist, *Anal. Chem.*, 2000, **72**, 1645–1648.
37 J. Kuligowski, G. Quintas and B. Lendl, *Appl. Phys. B: Lasers Opt.*, 2010, **99**, 833–840.
38 Y. Wang, M. G. Soskind, W. Wang and G. Wysocki, *Appl. Phys. Lett.*, 2014, **104**, 031114.
39 L. Diehl, C. Pflügl, M. F. Witinski, P. Wang, T. J. Tague and F. Capasso, Fourier transform spectrometers utilizing mid-infrared Quantum Cascade Lasers, CLEO/QELS: 2010 Laser Science to Photonic Applications, 2010.
40 P. Fuchs, J. Friedl, S. Hofling, J. Koeth, A. Forchel and L. Worschech, *et al.*, *Opt. Express*, 2012, **20**, 3890–3897.
41 J. P. Waclawek, R. Lewicki, H. Moser, M. Brandstetter, F. K. Tittel and B. Lendl, *Appl. Phys. B: Lasers Opt.*, 2014, **117**, 113–120.
42 C. Reidl-Leuthner, A. Viernstein, K. Wieland, W. Tomischko, L. Sass and G. Kinger, *et al.*, *Anal. Chem.*, 2014, **86**, 9058–9064.
43 G. Duxbury, N. Langford, M. T. McCulloch and S. Wright, *Chem. Soc. Rev.*, 2005, **34**, 921–934.
44 B. G. Lee, M. A. Belkin, C. Pflugl, L. Diehl, H. F. A. Zhang and R. M. Audet, *et al.*, *IEEE J. Quantum Electron.*, 2009, **45**, 554–565.
45 B. G. Lee, H. A. Zhang, C. Pflugl, L. Diehl, M. A. Belkin and M. Fischer, *et al.*, *IEEE Photonics Technol. Lett.*, 2009, **21**, 914–916.
46 R. Lewicki, M. Witinski, B. Li and G. Wysocki, *Spectroscopic benzene detection using a broadband monolithic DFB-QCL array*, SPIE, San Francisco, USA, 2016.
47 P. Rauter and F. Capasso, *Laser Photonics Rev.*, 2015, **9**, 452–477.
48 M. R. Alcaráz, A. Schwaighofer, H. Goicoechea and B. Lendl, *Anal. Bioanal. Chem.*, 2016, **408**, 3933–3941.
49 E. Mujagic, S. Schartner, L. K. Hoffmann, W. Schrenk, M. P. Semtsiv and M. Wienold, *et al.*, *Appl. Phys. Lett.*, 2008, **93**, 011108.
50 E. Mujagic, M. Nobile, H. Detz, W. Schrenk, J. X. Chen and C. Gmachl, *et al.*, *Appl. Phys. Lett.*, 2010, **96**, 031111.
51 M. Brandstetter, A. Genner, C. Schwarzer, E. Mujagic, G. Strasser and B. Lendl, *Opt. Express*, 2014, **22**, 2656–2664.
52 E. Mujagic, L. K. Hoffmann, S. Schartner, M. Nobile, W. Schrenk and M. P. Semtsiv, *et al.*, *Appl. Phys. Lett.*, 2008, **93**, 161101.
53 H. Moser, A. Genner, J. Ofner, C. Schwarzer, G. Strasser and B. Lendl, *Opt. Express*, 2016, **24**, 6572–6585.
54 G. Wysocki, R. F. Curl, F. K. Tittel, R. Maulini, J. M. Bulliard and J. Faist, *Appl. Phys. B: Lasers Opt.*, 2005, **81**, 769–777.
55 G. P. Luo, C. Peng, H. Q. Le, S. S. Pei, W. Y. Hwang and B. Ishaug, *et al.*, *Appl. Phys. Lett.*, 2001, **78**, 2834–2836.
56 G. Totschnig, F. Winter, V. Pustogov, J. Faist and A. Muller, *Opt. Lett.*, 2002, **27**, 1788–1790.
57 M. Beck, D. Hofstetter, T. Aellen, J. Faist, U. Oesterle and M. Ilegems, *et al.*, *Science*, 2002, **295**, 301–305.
58 S. Riedi, A. Hugi, A. Bismuto, M. Beck and J. Faist, *Appl. Phys. Lett.*, 2013, **103**, 031108.
59 K. Yeh, S. Kenkel, J.-N. Liu and R. Bhargava, *Anal. Chem.*, 2014, **87**, 485–493.
60 F. Lu and M. A. Belkin, *Opt. Express*, 2011, **19**, 19942–19947.
61 G. Ramer, A. Balbekova, A. Schwaighofer and B. Lendl, *Anal. Chem.*, 2015, **87**, 4415–4420.
62 F. Fuchs, S. Hugger, M. Kinzer, R. Aidam, W. Bronner and R. Losch, *et al.*, *Opt. Eng.*, 2010, **49**, 111127.
63 M. Brandstetter, A. Genner, K. Anic and B. Lendl, *Analyst*, 2010, **135**, 3260–3265.
64 A. Schwaighofer, M. R. Alcaraz, C. Araman, H. Goicoechea and B. Lendl, *Sci. Rep.*, 2016, **6**, 33556.
65 Á. I. López-Lorente, P. Wang, M. Sieger, E. Vargas Catalan, M. Karlsson and F. Nikolajeff, *et al.*, *Phys. Status Solidi A*, 2016, **213**, 2117–2123.
66 S. D. Saliba, M. Junker, L. D. Turner and R. E. Scholten, *Appl. Opt.*, 2009, **48**, 6692–6700.
67 M. Yamada, *IEEE J. Quantum Electron.*, 1986, **22**, 1052–1059.
68 F. Fuchs, B. Kirn, C. Mann, Q. Yang, W. Bronner and B. Raynor, *et al.*, *Spectral tuning and mode competition of quantum cascade lasers studied by time-resolved Fourier transform spectroscopy*, SPIE, Boston, USA, 2006.
69 G. Wysocki, R. Lewicki, R. F. Curl, F. K. Tittel, L. Diehl and F. Capasso, *et al.*, *Appl. Phys. B: Lasers Opt.*, 2008, **92**, 305–311.
70 R. Centeno, D. Marchenko, J. Mandon, S. M. Cristescu, G. Wulterkens and F. J. M. Harren, *Appl. Phys. Lett.*, 2014, **105**, 261907.
71 R. Maulini, *Broadly tunable mid-infrared quantum cascade lasers for spectroscopic applications*, VDM Verlag Dr Müller, Saarbrücken, 2009.
72 T. Berer, M. Brandstetter, A. Hochreiner, G. Langer, W. Marzinger and P. Burgholzer, *et al.*, *Opt. Lett.*, 2015, **40**, 3476–3479.
73 M. Brandstetter, L. Volgger, A. Genner, C. Jungbauer and B. Lendl, *Appl. Phys. B: Lasers Opt.*, 2013, **110**, 233–239.
74 M. R. Alcaráz, A. Schwaighofer, C. Kristament, G. Ramer, M. Brandstetter and H. Goicoechea, *et al.*, *Anal. Chem.*, 2015, **87**, 6980–6987.
75 A. Ogunleke, V. Bobroff, H.-H. Chen, J. Rowlette, M. Delugin and B. Recur, *et al.*, *TrAC, Trends Anal. Chem.*, 2017, **89**, 190–196.

76 J. Faist, C. Gmachl, F. Capasso, C. Sirtori, D. L. Sivco and J. N. Baillargeon, *et al.*, *Appl. Phys. Lett.*, 1997, **71**, 986.
77 M. S. Taubman, T. L. Myers, B. D. Cannon and R. M. Williams, *Spectrochim. Acta, Part A*, 2004, **60**, 3457–3468.
78 M. G. Hansen, E. Magoulakis, Q. F. Chen, I. Ernsting and S. Schiller, *Opt. Lett.*, 2015, **40**, 2289–2292.
79 S. Welzel, F. Hempel, M. Hubner, N. Lang, P. B. Davies and J. Ropcke, *Sensors*, 2010, **10**, 6861–6900.
80 J. Hodgkinson and R. P. Tatam, *Meas. Sci. Technol.*, 2013, **24**, 012004.
81 G. Hancock, J. H. van Helden, R. Peverall, G. A. D. Ritchie and R. J. Walker, *Appl. Phys. Lett.*, 2009, **94**, 201110.
82 J. Ropcke, P. B. Davies, N. Lang, A. Rousseau and S. Welzel, *J. Phys. D: Appl. Phys.*, 2012, **45**, 423001.
83 M. Brandstetter, C. Koch, A. Genner and B. Lendl, *Proc. SPIE*, 2014, **8993**, 89931u.
84 M. Brandstetter and B. Lendl, *Sens. Actuators, B*, 2012, **170**, 189–195.
85 M. T. McCulloch, E. L. Normand, N. Langford, G. Duxbury and D. A. Newnham, *J. Opt. Soc. Am. B*, 2003, **20**, 1761–1768.
86 K. Haase, N. Kroger-Lui, A. Pucci, A. Schonhals and W. Petrich, *Faraday Discuss.*, 2015, **187**, 119–134.
87 N. Kröger, A. Egl, M. Engel, N. Gretz, K. Haase and I. Herpich, *et al.*, *J. Biomed. Opt.*, 2014, **19**, 111607.
88 K. Yeh and R. Bhargava, *Proc. SPIE*, 2016, **9704**, 970406.
89 T. Stangier, G. Sonnabend and M. Sornig, *Remote Sens.*, 2013, **5**, 3397–3414.
90 N. A. Macleod and D. Weidmann, *Proc. SPIE*, 2012, **8546**, 85460h.
91 M. Nikodem, C. Smith, D. Weidmann and G. Wysocki, *Proc. SPIE*, 2011, **8024**, 80240f.
92 M. Sieger, F. Balluff, X. Wang, S.-S. Kim, L. Leidner and G. Gauglitz, *et al.*, *Anal. Chem.*, 2013, **85**, 3050–3052.
93 J. Hayden, S. Hugger, F. Fuchs and B. Lendl, *Appl. Phys. B: Lasers Opt.*, 2017, submitted.
94 G. Wysocki and D. Weidmann, *Opt. Express*, 2010, **18**, 26123–26140.
95 C. S. Colley, J. C. Hebden, D. T. Delpy, A. D. Cambrey, R. A. Brown and E. A. Zibik, *et al.*, *Rev. Sci. Instrum.*, 2007, **78**, 123108.
96 D. Varnell, M. C. Zheng, C. F. Gmachl and M. Chow, Spectroscopy and Imaging Using a Mid-IR Quantum Cascade Optical Coherence Tomography (OCT) System, Conference on Lasers and Electro-Optics, 2016.
97 T. Udem, R. Holzwarth and T. W. Hansch, *Nature*, 2002, **416**, 233–237.
98 J. Faist, G. Villares, G. Scalari, M. Rosch, C. Bonzon and A. Hugi, *et al.*, *Nanophotonics*, 2016, **5**, 272–291.
99 A. Hugi, G. Villares, S. Blaser, H. C. Liu and J. Faist, *Nature*, 2012, **492**, 229–233.
100 I. Coddington, N. Newbury and W. Swann, *Optica*, 2016, **3**, 414–426.
101 G. Villares, A. Hugi, S. Blaser and J. Faist, *Nat. Commun.*, 2014, **5**, 5192.
102 D. D. Coon and R. P. G. Karunasiri, *Appl. Phys. Lett.*, 1984, **45**, 649–651.
103 H. C. Liu, M. Buchanan and Z. R. Wasilewski, *Appl. Phys. Lett.*, 1998, **72**, 1682–1684.
104 C. Wieman and T. W. Hansch, *Phys. Rev. Lett.*, 1976, **36**, 1170–1173.
105 S. Lüdeke, M. Pfeifer and P. Fischer, *J. Am. Chem. Soc.*, 2011, **133**, 5704–5707.
106 N. F. Yu, Q. J. Wang, C. Pflugl, L. Diehl, F. Capasso and T. Edamura, *et al.*, *Appl. Phys. Lett.*, 2009, **94**, 151101.
107 S. Law, V. Podolskiy and D. Wasserman, *Nanophotonics*, 2013, **2**, 103–130.
108 N. Yu, Q. Wang and F. Capasso, *Laser Photonics Rev.*, 2012, **6**, 24–46.
109 D. Dhirhe, T. J. Slight, B. M. Holmes and C. N. Ironside, *Opt. Express*, 2013, **21**, 24267–24280.
110 Z. Bielecki, T. Stacewicz, J. Wojtas and J. Mikolajczyk, *Bull. Pol. Acad. Sci.: Tech. Sci.*, 2015, **63**, 515–525.
111 J. Mikolajczyk, Z. Bielecki, T. Stacewicz, J. Smulko, J. Wojtas and D. Szabra, *et al.*, *Metrol. Meas. Syst.*, 2016, **23**, 205–224.
112 A. Amann, W. Miekisch, J. Schubert, B. Buszewski, T. Ligor and T. Jezierski, *et al.*, *Annu. Rev. Anal. Chem.*, 2014, **7**, 455–482.
113 T. H. Risby and F. K. Tittel, *Opt. Eng.*, 2010, **49**, 111123.
114 F. K. Tittel, D. Richter and A. Fried, in *Solid-State Mid-Infrared Laser Sources*, ed. I. T. Sorokina and K. L. Vodopyanov, Springer-Verlag Berlin Heidelberg, 2003, vol. 89, pp. 445–510.
115 C. J. Wang and P. Sahay, *Sensors*, 2009, **9**, 8230–8262.
116 B. Buszewski, M. Kesy, T. Ligor and A. Amann, *Biomed. Chromatogr.*, 2007, **21**, 553–566.
117 C. Turner, *Bioanalysis*, 2016, **8**, 677–690.
118 J. D. Pleil, M. A. Stiegel and T. H. Risby, *J. Breath Res.*, 2013, **7**, 017107.
119 A. S. Modak, *J. Breath Res.*, 2007, **1**, 014003.
120 P. D. Klein, *J. Nutr.*, 2001, **131**, 1637s–1642s.
121 Y. C. Luiking and N. E. P. Deutz, *Curr. Opin. Clin. Nutr. Metab. Care*, 2003, **6**, 103–108.
122 P. Krumbiegel, E. Denk, R. Russow, U. Rolle-Kampczyk, G. Metzner and O. Herbarth, *Exp. Lung Res.*, 2002, **28**, 535–542.
123 W. Q. Cao and Y. X. Duan, *Crit. Rev. Anal. Chem.*, 2007, **37**, 3–13.
124 M. Haisch, P. Hering, W. Fuss and W. Fabinski, *Isotopenpraxis*, 1994, **30**, 247–251.
125 J. B. Mcmanus, M. S. Zahniser, D. D. Nelson, L. R. Williams and C. E. Kolb, *Spectrochim. Acta, Part A*, 2002, **58**, 2465–2479.
126 M. Erdelyi, D. Richter and F. K. Tittel, *Appl. Phys. B: Lasers Opt.*, 2002, **75**, 289–295.
127 J. F. Becker, T. B. Sauke and M. Loewenstein, *Appl. Opt.*, 1992, **31**, 1921–1927.
128 D. Weidmann, G. Wysocki, C. Oppenheimer and F. K. Tittel, *Appl. Phys. B: Lasers Opt.*, 2005, **80**, 255–260.
129 T. Rubin, T. von Haimberger, A. Helmke and K. Heyne, *J. Breath Res.*, 2011, **5**, 027102.
130 V. L. Kasyutich and P. A. Martin, *Infrared Phys. Technol.*, 2012, **55**, 60–66.

131 K. Worle, F. Seichter, A. Wilk, C. Armacost, T. Day and M. Godejohann, *et al.*, *Anal. Chem.*, 2013, **85**, 2697–2702.
132 Y. Wang, M. Nikodem, E. Zhang, F. Cikach, J. Barnes and S. Comhair, *et al.*, *Sci. Rep.*, 2015, **5**, 9096.
133 Y. Wang, M. Nikodem, R. Dweik and G. Wysocki, A Dual Modulation Faraday Rotation Spectrometer for Isotope-Labeled Analysis of Exhaled Nitric Oxide, *Opt. Life Sci.*, 2013, BM4A.3.
134 Y. Wang, F. Cikach, J. Barnes, L. Dababneh, D. Grove and S. Erzurum, *et al.*, A Faraday Rotation Spectrometer for study of NO isotopes in breath, 2013 Conference on Lasers and Electro-Optics (Cleo), 2013.
135 Z. N. Wang and C. J. Wang, *J. Breath Res.*, 2013, **7**, 037109.
136 L. Ciaffoni, G. Hancock, J. J. Harrison, J. P. van Helden, C. E. Langley and R. Peverall, *et al.*, *Anal. Chem.*, 2013, **85**, 846–850.
137 A. Reyes-Reyes, R. C. Horsten, H. P. Urbach and N. Bhattacharya, *Anal. Chem.*, 2015, **87**, 507–512.
138 S. W. Ryter and L. E. Otterbein, *BioEssays*, 2004, **26**, 270–280.
139 S. W. Ryter and A. M. K. Choi, *J. Breath Res.*, 2013, **7**, 017111.
140 B. W. M. Moeskops, H. Naus, S. M. Cristescu and F. J. M. Harren, *Appl. Phys. B: Lasers Opt.*, 2006, **82**, 649–654.
141 N. Pakmanesh, S. M. Cristescu, A. Ghorbanzadeh, F. J. M. Harren and J. Mandon, *Appl. Phys. B: Lasers Opt.*, 2016, **122**, 10.
142 R. Ghorbani and F. M. Schmidt, *Appl. Phys. B: Lasers Opt.*, 2017, **123**, 144.
143 C. Turner, P. Spanel and D. Smith, *Physiol. Meas.*, 2006, **27**, 321–337.
144 C. D. R. Dunn, M. Black, D. C. Cowell, C. Penault, N. M. Ratcliffe and R. Spence, *et al.*, *Br. J. Biomed. Sci.*, 2001, **58**, 66–75.
145 J. Manne, O. Sukhorukov, W. Jager and J. Tulip, *Appl. Opt.*, 2006, **45**, 9230–9237.
146 J. Manne, W. Jager and J. Tulip, *Appl. Phys. B: Lasers Opt.*, 2009, **94**, 337–344.
147 R. Lewicki, A. A. Kosterev, D. M. Thomazy, T. H. Risby, S. Solga and T. B. Schwartz, *et al.*, *Proc. SPIE*, 2011, **7945**, 79450k.
148 F. K. Tittel, R. F. Curl, L. Dong and R. Lewicki, *Infrared semiconductor laser based trace gas sensor technologies: recent advances and applications*, 2011.
149 F. K. Tittel, R. Lewicki, L. Dong, K. Liu, T. H. Risby and S. Solga, *et al.*, *Real time detection of exhaled human breath using quantum cascade laser based sensor technology*, 2012.
150 K. Owen and A. Farooq, *Appl. Phys. B: Lasers Opt.*, 2014, **116**, 371–383.
151 B. Gaston, J. M. Drazen, J. Loscalzo and J. S. Stamler, *Am. J. Respir. Crit. Care Med.*, 1994, **149**, 538–551.
152 D. H. Yates, *Immunol. Cell Biol.*, 2001, **79**, 178–190.
153 N. Binding, W. Muller, P. A. Czeschinski and U. Witting, *Eur. Respir. J.*, 2000, **16**, 499–503.
154 J. H. Shorter, D. D. Nelson, J. B. McManus, M. S. Zahniser, S. R. Sama and D. K. Milton, *J. Breath Res.*, 2011, **5**, 037108.
155 L. Menzel, A. A. Kosterev, R. F. Curl, F. K. Tittel, C. Gmachl and F. Capasso, *et al.*, *Appl. Phys. B: Lasers Opt.*, 2001, **72**, 859–863.
156 S. M. Cristescu, S. T. Persijn, S. T. L. Hekkert and F. J. M. Harren, *Appl. Phys. B: Lasers Opt.*, 2008, **92**, 343–349.
157 J. Mandon, M. Hogman, J. F. M. Merkus, J. van Amsterdam, F. J. M. Harren and S. M. Cristescu, *J. Biomed. Opt.*, 2012, **17**, 017003.
158 Y. A. Bakhirkin, A. A. Kosterev, C. Roller, R. F. Curl and F. K. Tittel, *Appl. Opt.*, 2004, **43**, 2257–2266.
159 M. L. Silva, D. M. Sonnenfroh, D. I. Rosen, M. G. Allen and A. O. Keefe, *Appl. Phys. B: Lasers Opt.*, 2005, **81**, 705–710.
160 M. R. McCurdy, Y. A. Bakhirkin and F. K. Tittel, *Appl. Phys. B: Lasers Opt.*, 2006, **85**, 445–452.
161 M. R. McCurdy, Y. Bakhirkin, G. Wysocki and F. K. Tittel, *J. Biomed. Opt.*, 2007, **12**, 034034.
162 D. Marchenko, J. Mandon, S. M. Cristescu, P. Merkus and F. J. M. Harren, *Appl. Phys. B: Lasers Opt.*, 2013, **111**, 359–365.
163 J. Wojtas, *Sensors*, 2015, **15**, 14356–14369.
164 A. De, G. D. Banik, A. Maity, M. Pal and M. Pradhan, *Opt. Lett.*, 2016, **41**, 1949–1952.
165 J. H. Shorter, D. D. Nelson, J. B. McManus, M. S. Zahniser and D. K. Milton, *IEEE Sens. J.*, 2010, **10**, 76–84.
166 A. Reyes-Reyes, Z. Hou, E. van Mastrigt, R. C. Horsten, J. C. de Jongste and M. W. Pijnenburg, *et al.*, *Opt. Express*, 2014, **22**, 18299–18309.
167 E. Mastrigt, A. Reyes-Reyes, K. Brand, N. Bhattacharya, H. P. Urbach and A. P. Stubbs, *et al.*, *J. Breath Res.*, 2016, **10**, 026003.
168 M. J. Pilling, A. Henderson, B. Bird, M. D. Brown, N. W. Clarke and P. Gardner, *Faraday Discuss.*, 2016, **187**, 135–154.
169 J. B. Lattouf and F. Saad, *BJU Int.*, 2002, **90**, 694–698.
170 M. J. Walsh, R. K. Reddy and R. Bhargava, *IEEE J. Sel. Top. Quantum Electron.*, 2012, **18**, 1502–1513.
171 A. Akalin, X. Y. Mu, M. A. Kon, A. Ergin, S. H. Remiszewski and C. M. Thompson, *et al.*, *Lab. Invest.*, 2015, **95**, 697.
172 E. Gazi, M. Baker, J. Dwyer, N. P. Lockyer, P. Gardner and J. H. Shanks, *et al.*, *Eur. Urol.*, 2006, **50**, 750–761.
173 N. Wald and E. Goormaghtigh, *Analyst*, 2015, **140**, 2144–2155.
174 R. Wolthuis, A. Travo, C. Nicolet, A. Neuville, M.-P. Gaub and D. Guenot, *et al.*, *Anal. Chem.*, 2008, **80**, 8461–8469.
175 A. Travo, O. Piot, R. Wolthuis, C. Gobinet, M. Manfait and J. Bara, *et al.*, *Histopathology*, 2010, **56**, 921–931.
176 R. Bhargava and A. Madabhushi, *Annu. Rev. Biomed. Eng.*, 2016, **18**, 387–412.
177 M. Pilling and P. Gardner, *Chem. Soc. Rev.*, 2016, **45**, 1935–1957.
178 R. Bhargava, *Appl. Spectrosc.*, 2012, **66**, 1091–1120.
179 P. Bassan, M. J. Weida, J. Rowlette and P. Gardner, *Analyst*, 2014, **139**, 3856–3859.
180 C. Hughes, G. Clemens, B. Bird, T. Dawson, K. M. Ashton and M. D. Jenkinson, *et al.*, *Sci. Rep.*, 2016, **6**, 20173.
181 T. P. Wrobel, M. R. Kole and R. Bhargava, *Spectroscopy*, 2016, **31**, 28–45.
182 M. R. Kole, R. K. Reddy, M. V. Schulmerich, M. K. Gelber and R. Bhargava, *Anal. Chem.*, 2012, **84**, 10366–10372.

183 M. C. Phillips and N. Ho, *Opt. Express*, 2008, **16**, 1836–1845.
184 B. Guo, Y. Wang, C. Peng, G. P. Luo and H. Q. Le, *Appl. Spectrosc.*, 2003, **57**, 811–822.
185 S. Tiwari, J. Raman, V. Reddy, A. Ghetler, R. P. Tella and Y. Han, *et al.*, *Anal. Chem.*, 2016, **88**, 10183–10190.
186 N. Kröger, A. Egl, M. Engel, N. Gretz, K. Haase and I. Herpich, *et al.*, Rapid hyperspectral imaging in the mid-infrared, Progress in Biomedical Optics and Imaging – Proceedings of SPIE, 2014.
187 N. Kröger-Lui, N. Gretz, K. Haase, B. Kranzlin, S. Neudecker and A. Pucci, *et al.*, *Analyst*, 2015, **140**, 2086–2092.
188 K. Haase, N. Kröger-Lui, A. Pucci, A. Schönhals and W. Petrich, *J. Biophotonics*, 2016, **9**, 61–66.
189 N. Kröger-Lui, K. Haase, A. Pucci, A. Schonhals and W. Petrich, *Proc. SPIE*, 2016, **9704**, 97040j.
190 G. Clemens, B. Bird, M. Weida, J. Rowlette and M. J. Baker, *Spectrosc. Eur.*, 2014, **26**, 14–19.
191 H. Sreedhar, V. K. Varma, F. V. Gambacorta, G. Guzman and M. J. Walsh, *Biomed. Opt. Express*, 2016, **7**, 2419–2424.
192 B. Bird and J. Rowlette, *Analyst*, 2017, **142**, 1381–1386.
193 *Vibrational Spectroscopy in Life Science*, ed. F. Siebert and P. Hildebrandt, Wiley-VCH Verlag GmbH & Co. KGaA, Weinheim, 2008.
194 S. K. Vashist, *Anal. Chim. Acta*, 2012, **750**, 16–27.
195 C. E. F. do Amaral and B. Wolf, *Med. Eng. Phys.*, 2008, **30**, 541–549.
196 C. Chen, X. L. Zhao, Z. H. Li, Z. G. Zhu, S. H. Qian and A. J. Flewitt, *Sensors*, 2017, **17**, 182.
197 C. Andreea, H. Cristina and S. Rafael, *Curr. Diabetes Rev.*, 2012, **8**, 48–54.
198 N. S. Oliver, C. Toumazou, A. E. G. Cass and D. G. Johnston, *Diabetic Med.*, 2009, **26**, 197–210.
199 W. B. Martin, S. Mirov and R. Venugopalan, *Appl. Spectrosc.*, 2005, **59**, 881–884.
200 M. Brandstetter, A. Genner, K. Anic and B. Lendl, *Procedia Eng.*, 2010, **5**, 1001–1004.
201 M. Brandstetter, T. Sumalowitsch, A. Genner, A. E. Posch, C. Herwig and A. Drolz, *et al.*, *Analyst*, 2013, **138**, 4022–4028.
202 A. Lambrecht, T. Beyer, K. Hebestreit, R. Mischler and W. Petrich, *Appl. Spectrosc.*, 2006, **60**, 729–736.
203 C. Herrmann, C. Vrancic, A. Fomichova, N. Gretz, S. Hoecker and A. Pucci, *et al.*, *Proc. SPIE*, 2010, **7560**, 75600e.
204 C. Vrancic, A. Fomichova, N. Gretz, C. Herrmann, S. Neudecker and A. Pucci, *et al.*, *Analyst*, 2011, **136**, 1192–1198.
205 C. Vrancic, N. Gretz, N. Kroger, S. Neudecker, A. Pucci and W. Petrich, *Proc. SPIE*, 2012, **8219**, 82190u.
206 C. Vrancic, N. Kroger, N. Gretz, S. Neudecker, A. Pucci and W. Petrich, *Anal. Chem.*, 2014, **86**, 10511–10514.
207 S. Liakat, K. A. Bors, T. Y. Huang, A. P. M. Michel, E. Zanghi and C. F. Gmachl, *Biomed. Opt. Express*, 2013, **4**, 1083–1090.
208 S. Liakat, K. A. Bors, L. Xu, C. M. Woods, J. Doyle and C. F. Gmachl, *Biomed. Opt. Express*, 2014, **5**, 2397–2404.
209 J. S. Li, B. Yu, H. Fischer, W. Chen and A. P. Yalin, *Rev. Sci. Instrum.*, 2015, **86**, 031501.
210 C. Haisch, *Meas. Sci. Technol.*, 2012, **23**, 012001.
211 H. von Lilienfeld-Toal, M. Weidenmuller, A. Xhelaj and W. Mantele, *Vib. Spectrosc.*, 2005, **38**, 209–215.
212 M. Pleitez, H. von Lilienfeld-Toal and W. Mantele, *Spectrochim. Acta, Part A*, 2012, **85**, 61–65.
213 M. A. Pleitez, T. Lieblein, A. Bauer, O. Hertzberg, H. von Lilienfeld-Toal and W. Mantele, *Anal. Chem.*, 2013, **85**, 1013–1020.
214 M. A. Pleitez, T. Lieblein, A. Bauer, O. Hertzberg, H. von Lilienfeld-Toal and W. Mantele, *Rev. Sci. Instrum.*, 2013, **84**, 084901.
215 M. A. Pleitez, O. Hertzberg, A. Bauer, M. Seeger, T. Lieblein and H. von Lilienfeld-Toal, *et al.*, *Analyst*, 2015, **140**, 483–488.
216 O. Hertzberg, A. Bauer, A. Kuderle, M. A. Pleitez and W. Mantele, *Analyst*, 2017, **142**, 495–502.
217 A. Bauer, O. Hertzberg, A. Küderle, D. Strobel, M. A. Pleitez and W. Mäntele, *J. Biophotonics*, 2017, DOI: 10.1002/jbio.201600261.
218 M. A. Pleitez, O. Hertzberg, A. Bauer, T. Lieblein, M. Glasmacher and H. Tholl, *et al.*, *Spectrochim. Acta, Part A*, 2017, **184**, 220–227.
219 J. Kottmann, J. M. Rey, J. Luginbuhl, E. Reichmann and M. W. Sigrist, *Biomed. Opt. Express*, 2012, **3**, 667–680.
220 J. Kottmann, U. Grob, J. M. Rey and M. W. Sigrist, *Sensors*, 2013, **13**, 535–549.
221 J. Kottmann, J. Rey and M. Sigrist, *Sensors*, 2016, **16**, 1663.
222 A. J. Jenkins, J. M. Oyler and E. J. Cone, *J. Anal. Toxicol.*, 1995, **19**, 359–374.
223 Y. C. Chang, P. Waegli, V. Paeder, A. Homsy, L. Hvozdara and P. van der Wal, *et al.*, *Lab Chip*, 2012, **12**, 3020–3023.
224 P. Wägli, Y.-C. Chang, A. Homsy, L. Hvozdara, H. P. Herzig and N. F. de Rooij, *Anal. Chem.*, 2013, **85**, 7558–7565.
225 P. Jouy, M. Mangold, B. Tuzson, L. Emmenegger, Y.-C. Chang and L. Hvozdara, *et al.*, *Analyst*, 2014, **139**, 2039–2046.
226 J. Kuligowski, A. Schwaighofer, M. R. Alcaráz, G. Quintás, H. Mayer and M. Vento, *et al.*, *Anal. Chim. Acta*, 2017, **963**, 99–105.
227 G. Villares, J. Wolf, D. Kazakov, M. J. Suess, A. Hugi and M. Beck, *et al.*, *Appl. Phys. Lett.*, 2015, **107**, 251104.
228 Y. Bidaux, A. Bismuto, C. Tardy, R. Terazzi, T. Gresch and S. Blaser, *et al.*, *Appl. Phys. Lett.*, 2015, **107**, 221108.
229 A. Bismuto, Y. Bidaux, C. Tardy, R. Terazzi, T. Gresch and J. Wolf, *et al.*, *Opt. Express*, 2015, **23**, 29715–29722.
230 A. Goyal, T. Myers, C. A. Wang, M. Kelly, B. Tyrrell and B. Gokden, *et al.*, *Opt. Express*, 2014, **22**, 14392–14401.
231 M. F. Witinski, R. Blanchard, C. Pfluegl, L. Diehl, B. Li and B. Pancy, *et al.*, *Laser Focus World*, 2015, **51**, 36–39.
232 F. R. Giorgetta, E. Baumann, M. Graf, Q. K. Yang, C. Manz and K. Kohler, *et al.*, *IEEE J. Quantum Electron.*, 2009, **45**, 1029–1042.
233 A. Harrer, R. Szedlak, B. Schwarz, H. Moser, T. Zederbauer and D. MacFarland, *et al.*, *Sci. Rep.*, 2016, **6**, 21795.
234 R. Szedlak, A. Harrer, M. Holzbauer, B. Schwarz, J. P. Waclawek and D. MacFarland, *et al.*, *ACS Photonics*, 2016, **3**, 1794–1798.
235 B. Schwarz, P. Reininger, D. Ristanic, H. Detz, A. M. Andrews and W. Schrenk, *et al.*, *Nat. Commun.*, 2014, **5**, 4085.
236 A. Dazzi and C. B. Prater, *Chem. Rev.*, 2016, **117**, 5146–5173.

237 A. Centrone, *Annu. Rev. Anal. Chem.*, 2015, **8**, 101–126.
238 S. Clede, F. Lambert, C. Sandt, S. Kascakova, M. Unger and E. Harte, *et al.*, *Analyst*, 2013, **138**, 5627–5638.
239 L. Baldassarre, V. Giliberti, A. Rosa, M. Ortolani, A. Bonamore and P. Baiocco, *et al.*, *Nanotechnology*, 2016, **27**, 075101.
240 H. Amrania, L. Drummond, R. C. Coombes, S. Shousha, L. Woodley-Barker and K. Weir, *et al.*, *Faraday Discuss.*, 2016, **187**, 539–553.
241 M. Brehm, T. Taubner, R. Hillenbrand and F. Keilmann, *Nano Lett.*, 2006, **6**, 1307–1310.
242 W. Petrich, *Faraday Discuss.*, 2016, **187**, 603–607.
243 M. J. Baker, S. R. Hussain, L. Lovergne, V. Untereiner, C. Hughes and R. A. Lukaszewski, *et al.*, *Chem. Soc. Rev.*, 2016, **45**, 1803–1818.
244 I. Pence and A. Mahadevan-Jansen, *Chem. Soc. Rev.*, 2016, **45**, 1958–1979.
245 G. Sun, in *Advances in Lasers and Electro Optics*, ed. N. Costa and A. Cartaxo, InTech, Rijeka, Croatia, 2010.
246 M. Troccoli, L. Diehl, D. P. Bour, S. W. Corzine, N. F. Yu and C. Y. Wang, *et al.*, *J. Lightwave Technol.*, 2008, **26**, 3534–3555.

